Article

Ni-M-O (M=Sn, Ti and W) catalysts prepared from dry mixing method for oxidative dehydrogenation of ethane

Haibo Zhu, Devon C. Rosenfeld, Moussab Harb, Dalaver H. Anjum, M. N. Hedhili, Samy Ould-Chikh, and Jean-Marie Basset

ACS Catal., **Just Accepted Manuscript** • DOI: 10.1021/acscatal.6b00044 • Publication Date (Web): 25 Mar 2016

Ni-M-O (M=Sn, Ti and W) catalysts prepared from dry mixing method for oxidative dehydrogenation of ethane

Haibo Zhu[a], *Devon C. Rosenfeld*[b], *Moussab Harb*[a], *Dalaver H. Anjum*[c], *Mohamed Nejib Hedhili*[c], *Samy Ould Chikh*[a], *Jean-Marie Basset* [*a]

[a] KAUST Catalysis Center, King Abdullah University of Science and Technology, Thuwal 4700, Kingdom of Saudi Arabia

[b]The Dow Chemical Company, 2301 N. Brazosport Blvd., Freeport, TX 77541, USA

[c] KAUST Core Lab, King Abdullah University of Science and Technology, Thuwal 4700, Kingdom of Saudi Arabia

ABSTRACT

A new generation of Ni-Sn-O, Ni-Ti-O, and Ni-W-O catalysts has been prepared by a solid state grinding method. In each case the doping metal varied from 2.5% to 20%. These catalysts exhibited higher activity and selectivity for ethane oxidative dehydrogenation (ODH) than conventionally prepared mixed oxides. Detailed characterisation was achieved using XRD, N_2 adsorption, H_2-TPR, SEM, TEM, and HAADF-STEM in order to study the detailed atomic structure and textural properties of the synthesized catalysts. Two kinds of typical structures are found in these mixed oxides, which are (major) "Ni_xM_yO" (M = Sn, Ti or W) solid solution phases (NiO crystalline structure with doping atom incorporated in the lattice) and (minor) secondary phases (SnO_2, TiO_2 or WO_3). The secondary phase exists as a thin layer around small "Ni_xM_yO" particles, lowering the aggregation of nanoparticles during the synthesis. DFT calculations on the formation energies of M-doped NiO structures (M = Sn, Ti, W) clearly confirm the thermodynamic feasibility of incorporating these doping metals into NiO struture. The incorporation of doping metals into the NiO lattice decreases the number of holes (h^+) localized on lattice oxygen ($O^{2-} + h^+ \rightarrow O^{\bullet -}$), which is the main reason for the improved catalytic performance ($O^{\bullet -}$ is known to favor complete ethane oxidation to CO_2). The high efficiency of ethylene production achieved in these particularly prepared mixed oxide catalysts indicates that the solid grinding method could serve as a general and practical approach for the preparation of doped NiO based catalysts.

KEYWORDS: Solid state synthesis, NiO, semiconductor, ethylene production, oxidative dehydrogenation, single atom

1. Introduction

Ethylene is regarded as a very important raw material for the synthesis of a wide variety of products including polymers, fine chemicals, plastics, and fibers. Its primary use is in the production of polyethylene, which is the most widely used plastic in the world. In fact, ethylene is the highest volume chemical produced by the petrochemical industry[1] and is primarily produced by the steam cracking of hydrocarbon feedstock such as ethane and naphtha. The shortcomings of steam cracking are low olefin selectivity, raw material loss through coke formation requiring shut downs and maintenance and the large energy demand. In fact, ethylene production by the steam cracking process (at T>800°C) is considered one of the most energy intensive processes in the petrochemical industry.[2]

With worldwide ethylene demand expected to steadily increase each year for the foreseeable future, there is an increased focus on the development of new and improved technologies and processes for ethylene production. The catalytic oxidative dehydrogenation (ODH) of ethane is an attractive alternative technology for the production of ethylene.[3] Firstly, ODH is an exothermic process and this reaction is carried out at relatively low temperature (typically below 450 °C) in comparison with the steam cracking process.[4] Therefore, the ethylene production from ethane ODH could save a large amount of energy. Secondly, the large scale exploitation of shale gas has greatly increased the supply and lowered the cost of ethane. Lastly, catalyst deactivation from coke formation in the classical steam reforming process is suppressed due to the presence of oxygen and lower temperature operation.[5]

A great variety of metal oxide materials are efficient catalysts for the ethane ODH reaction.[6] Among these oxides, NiO based materials exhibit high activity and selectivity along with good

stability in ethane ODH, especially at temperatures <450 °C. Despite the superior low temperature ODH performance of NiO based materials further studies are necessary to assess their potential for use beyond the laboratory scale. The properties of NiO including ODH performance can be systematically tuned by doping with a secondary metal. The incorporation of "dopants' such as Nb,[7a-e] W,[8] Zr[9], Sn[10] and Ta[7f] into NiO results in formation of a new type of bimetallic oxide solid solution. The properties and catalytic performance of doped NiO are affected not only by the identity of the dopant but also by the method used to prepare the mixed metal oxide. We have shown that the Ni-Nb-O and Ni-Ta-O synthesized from a sol-gel method exhibits higher ethylene selectivities than those obtained by an evaporation or precipitation method.[7c, 7f] Furthermore, we have recently developed a more effective and sustainable method for the synthesis of Ni-Nb-O and Ni-Ta-O catalyst by a simple dry grinding of Ni and Nb or Ta precursors.[11] This "***solid state grinding***" synthetic method is green since it does not require any solvent, even water, in the preparation procedure, which shows great benefit in the practical application. In this paper, we found that this grinding method could be also extended to the synthesis of Ni-Ti-O, Ni-Sn-O and Ni-W-O catalysts, proving that "***solid state grinding"*** could serve as a general and versatile approach for the preparation of doped NiO. Full characterization of the mixed oxides and DFT calculations allow us to propose a theory on the origin of improved ethylene selectivity in ODH with this new generation of dopants.

2. Experimental Section

2.1 Catalysis synthesis

A dry solid state procedure was used to synthesize three series of Ni-Sn-O, Ni-Ti-O and Ni-W-O, catalysts with the doping metal atomic content of 2.5%, 5%, 10%, 15% and 20% in each

series. The following preparations are typical examples of the synthesis of $Ni_{0.95}M_{0.05}O$ (M=W, Ti and Sn) catalysts. (1) Synthesis of $Ni_{0.95}W_{0.05}O$ catalyst: 8.20 g of tungsten (VI) ethoxide in ethanol solution ($W(OCH_2CH_3)_6$, 5% w/v in ethanol) was dried at 70 °C to evaporate ethanol. The obtained powder was then mixed with 4.74 g of nickel nitrate hexahydrate ($Ni(NO_3)_2.6H_2O$) and 1.13g of oxalic acid ($H_2C_2O_4$) in a mortar bowl. Subsequently, the mixture was mixed and ground in the mortar bowl by using a pestle at room temperature (nominally 25 °C) for 30 minutes to get a uniform paste, and this paste was submitted to a drying process at 90 °C for 2 hours. Finally, the dried paste was calcined under static air at 300 °C for 4 hours to produce a black solid. (2) Synthesis of $Ni_{0.95}Ti_{0.05}O$ catalyst: Replicate the synthesis of $Ni_{0.95}W_{0.05}O$ substituting tungsten(VI) ethoxide with 0.20 g of titanium ethoxide ($Ti(OCH_2CH_3)_4$) in the synthesis. (3) Synthesis of $Ni_{0.95}Sn_{0.05}O$ catalyst: Replicate the synthesis of $Ni_{0.95}W_{0.05}O$ substituting tungsten(VI) ethoxide with 0.30 g of tin(IV) acetate ($Sn(CH_3CO_2)_4$) in the synthesis.

2.2 Catalysts characterization

X-ray diffraction (XRD) measurements were recorded using a Bruker D8 Advanced A25 diffractometer with Cu Kα radiation (λ=1.5406 Å) at 40 kV and 40 mA. The data sets were collected in step-scan mode over the 2θ range 10-90°, using a step interval of 0.05° and a counting time of 1s per step.

N_2 adsorption/desorption isotherms were carried out on a Micromeritics@ ASAP2420 instrument at 77 K. The samples were degassed in vacuum for 2 h at 150 °C before measurement. Surface area of the samples were evaluated by the multipoint BET analysis method in the P/P_0= 0.05-0.30 pressure range.

The temperature-programmed reduction (TPR) experiments were performed with an Altamira Instrument equipped with a thermal conductivity detector (TCD), and the acquired data were analyzed using the AMI software provided by the instrument company. 50 mg of fresh sample was loaded in a U-shaped quartz tube, and then was pretreated under high purity (99.9%) argon (30 ml min^{-1}) at 350 °C for 4 hours in order to remove adsorbed water and gas. Prior to the test, the sample was cooled down to the ambient temperature. Standard TPR analysis was done under 5% H_2/Ar with a flow of 30 mL min^{-1} from room temperature to 1100 °C with a ramp rate of 20 °C min^{-1}.

XPS studies were carried out in a Kratos Axis Ultra DLD spectrometer equipped with a monochromatic Al Kα x-ray source (hν=1486.6 eV) operating at 150 W, a multichannel plate and delay line detector under a vacuum of $1\sim10^{-9}$ mbar . The survey and high-resolution spectra were collected at fixed analyzer pass energies of 160 eV and 20 eV, respectively and quantified using empirically derived relative sensitivity factors provided by Kratos analytical. Samples were mounted in floating mode in order to avoid differential charging. Charge neutralization was required for all samples. Binding energies were referenced to the C 1s peak of (C-C, C-H) bond which was set at 284.8 eV. The data were analyzed with commercially available software, CasaXPS.

The morphologies of the catalysts were analyzed using an FEI Quanta 600 FEG environmental scanning electron microscope (ESEM). Each sample was sputter-coated with gold under an argon atmosphere before the SEM image was taken.

Low magnification transmission electron microscopy (TEM) images were obtained on a Tecnai T12 operated at 120 kV. While, the high resolution TEM and HAADF-STEM were conducted on

aberration corrected Ttitan G2 80-300 ST instrument. Samples were dispersed in ethanol with the help of ultrasound treatment, and then supported onto a 200 mesh carbon coated copper grid before TEM measurement.

2.3 Catalytic testing

The catalytic ethane ODH reaction was carried out using a fixed bed reactor operating at atmospheric pressure. 100 mg catalyst was introduced into the reactor with glass wool as support. The feedstock composed of 10% C_2H_6 and 5% O_2 in He was passed through the catalytic bed at a constant flow rate of 10 ml/min (W/F = 0.6 g s/mL). The evaluation of the catalyst performance was performed from 200 to 400 °C. The gas products were analyzed by an on-line Varian 490 micro-GC equipped with TCD detectors and two columns: MolSieve 5Å column (Ar as carrier gas) used to quantify O_2 (CO is not produced under our conditions), and a poraPLOT Q column (He as carrier gas) to analyze CO_2, C_2H_4 and C_2H_6. The ethane conversion and selectivity to ethylene were calculated on a carbon basis, and the carbon mass balance was above 96 % in all cases. In order to investigate ethane conversion versus ethylene selectivity at the constant temperature of 330 °C, the total flow rate was changed from 10 mL/min to 120 mL/min, corresponding to the W/F from 0.05 to 0.6 g s/mL.

3. Computational details

3.1. Supercell models and structure optimization calculations

For simulations of Ti-, Sn-, and W-doped NiO structures, we considered the (2 x 2 x 2) cubic NiO supercell (space group is FM-3M) containing 32 NiO functional units ($Ni_{32}O_{32}$) or 64 atoms. We modeled several structural configurations by substituting the dopant elements at various Ni sites accompanied by the removal of additional Ni species. For Ti-doped NiO, one

substitutional Ti at Ni sites in the presence of one or two additional Ni-vacancies (labeled by $1Ti_s@Ni+1V_{Ni}$ and $1Ti_s@Ni+2V_{Ni}$) were considered. For Sn-doped NiO, one substitutional Sn at Ni sites (labeled by $1Sn_s@Ni$) as well as one substitutional Sn at Ni sites in the presence of one or two additional Ni-vacancies (labeled by $1Sn_s@Ni+1V_{Ni}$ and $1Sn_s@Ni+2V_{Ni}$) were taken into account. For W-doped NiO, one substitutional W at Ni sites in the presence of two or three additional Ni-vacancies (labeled by $1W_s@Ni+2V_{Ni}$ and $1W_s@Ni+3V_{Ni}$) were studied. Note that for NiO, we also explored a defective structure in Ni (labeled by $1V_{Ni}$) which was modeled by removing one Ni from the $Ni_{32}O_{32}$ supercell, leading to the stoichiometry $Ni_{0.96}O$. For a generic supercell of doped NiO with the formula $Ni_{(32-k)}O_{32}M_p$(M = Ti, Sn and W) containing initially 64 atoms in total, and modified with p M atoms and k Ni vacancies, the atomic concentrations of M-impurities and of Ni-vacancies are defined as $y = \frac{p}{32}$ and $x = \frac{k}{32}$ respectively. In the $1Sn_s@Ni$ model, Sn^{2+} species are created, while in all the other structural models explored in our calculations, the oxidation states of the elements examined are Ti^{4+}, Sn^{4+} and W^{6+}. Note for NiO, Ni and O species are formally Ni^{2+} and O^{2-}. The various M-doped NiO materials considered in our calculations together with their stoichiometries are given in Table 1. Their structural configurations are displayed in Figure 1.

The various crystal structures were fully optimized using the spin-polarized periodic density functional theory (DFT) within the plane wave (PW) approach implemented in VASP program.[12] The generalized gradient approximation (GGA) within the Perdew-Burke-Emzerhof (PBE) exchange-correlation functional[13] and the projector-augmented plane wave (PAW) approach[14] were employed to describe the electron-electron and the electron-ion interactions, respectively. The valence atomic configurations adopted in PAW potentials are $3d^84s^2$ for Ni, $2s^22p^4$ for O,

$3d^34s^1$ for Ti,$5s^25p^2$ for Sn and $6s^25d^4$ for W. Cutoff energies of 400 eV and 605.4 eV were used for wave functions and charge augmentations, respectively. Integration of the band structure energy over the Brillouin zone was performed with the tetrahedron method with Blöchl corrections. In all cases, the Brillouin zone was sampled with 5 x 5 x 5 Monkhorst-Pack *k*-point grid.[15] The ion coordinates and lattice parameters were fully relaxed until all components of the residual forces were less than 0.01 eV/Å.

Table 1. Doping models and stoichiometries (including *p* and *k* values) of the various M-doped NiO materials (M = Ti, Sn and W) with 3 atom % of dopant impurities.

doping model	Structure	$Ni_{(32-k)}O_{32}M_p$ supercell model	$Ni_{(1-x)}OM_y$ stoichiometry
$1Ti_s@Ni+1V_{Ni}$	(1a)	*k*=2; *p*=1	$Ni_{0.93}Ti_{0.03}O$
$1Ti_s@Ni+2V_{Ni}$	(1b)	*k*=3; *p*=1	$Ni_{0.90}Ti_{0.03}O$
$1Sn_s@Ni+1V_{Ni}$	(1a)	*k*=2; *p*=1	$Ni_{0.93}Sn_{0.03}O$
$1Sn_s@Ni+2V_{Ni}$	(1b)	*k*=3; *p*=1	$Ni_{0.90}Sn_{0.03}O$
$1Sn_s@Ni$		*k*=1; *p*=1	$Ni_{0.96}Sn_{0.03}O$
$1W_s@Ni+2V_{Ni}$	(1c)	*k*=3; *p*=1	$Ni_{0.90}W_{0.03}O$
$1W_s@Ni+3V_{Ni}$	(1d)	*k*=4; *p*=1	$Ni_{0.87}W_{0.03}O$

3.2. Formation energy calculations

Identifying the thermodynamic feasibility of assembling the various explored materials from individual elements was performed by considering the following chemical reaction:

$$(1-x)\,Ni\,(s) + yM\,(s) + \tfrac{1}{2}O_2\,(g) \rightarrow Ni_{(1-x)}OM_{\ y}\,(s)\ \text{(M = Ti, Sn and W)}\ (1)$$

The formation energy (or reaction energy) was computed using the following expression:

$$E_{form} = E_{form}^{0K} - \Delta\mu_O (2)$$

where E_{form}^{0K} is the electronic energy at 0 K and expressed by:

$$E_{form}^{0K} = E_{tot}(Ni_{(1-x)}OM_y) - (1-x)E_{tot}(Ni) - yE_{tot}(M) - \tfrac{1}{2}E_{O_2} (3)$$

Equation (3) includes the total energies at 0 K for the $Ni_{(1-x)}OM_y$, Ni and M (Ti, Sn and W) solids in their ground-state structures as well as for the gas phase O_2 molecule. $\Delta\mu_O$ in equation (2) is the thermal part of the chemical potential of oxygen which depends on temperature (*T*) and pressure (*p*) *via* the enthalpy (*h*) and entropy (*s*) corrections as follows:

$$\Delta\mu_O = h_{O_2}(T) - Ts_{O_2}(T) + RTLn(\frac{p(O_2)}{p_0}) (4)$$

The zero point vibrational energy, the enthalpy correction (*h*) and the entropy(*s*) of O_2 as a function of the temperature (*T*) and the pressure (*p*) were calculated using DMolprogram[16] within the PBE exchange-correlation functional and the DNP basis set[17].The zero point vibrational energy was systematically included in the enthalpy and entropy corrections. The thermal contributions of the solids were neglected. All electronic energies (for solids and molecule) were calculated using VASP program. In what follows, $\Delta\mu_O$ was fixed at -0.22 eV for T = 298 K and $p(O_2)$ = 1 atm (standard thermodynamic conditions). Negative or positive formation energy corresponds to stable or unstable material. Lower or higher formation energy represents more or less stable material. Note that the formation energy for the defective NiO material ($Ni_{0.96}O$) was obtained from eq. (3) for y=0 and x=0.03.

4. Results and discussion

4.1 Catalyst characterization

We have prepared 3 groups of NiO based catalysts by the simple solid state method. In each group the doping metal content (atomic percentage) was changed systematically in the ranges of 2.5%, 5%, 10%, 15% and 20%. The XRD patterns of Ni-Ti-O, Ni-Sn-O and Ni-W-O materials are shown in Figure 2. All the samples show the strong diffraction peaks relevant to the crystal structure of the bunsenite NiO (JCPDS 78-0643).[7c, 9] These characteristic reflection peaks of NiO are located at 2θ around 37.1°, 43.2°, 62.5°, 74.8°, and 78.7°, which are due to the diffractions from (111), (200), (220), (311) and (222) planes, respectively. Actually, the width of the NiO diffraction peaks changes with the variation of doping metals loading. As the content of dopant increases, these reflection peaks become broad. The peaks widening suggests smaller crystallite sizes in the samples with higher dopant loading. The pure NiO reference prepared by a decomposition of $Ni(NO_3)_2$ has a mean crystallite size of 12 nm. In contrast to pure NiO, these mixed oxide samples have much smaller particle size. The particle size estimated using the Scherrer equation shown in Figure 3 clearly indicates an increase of doping metal loading leads to a decrease of particle size. With the increase of dopant content, the particle size of NiO reduces to around 4 nm in the samples with 20% dopant metal loading. As proposed by Millet et al. the decrease of particle size in mixed oxide could be due to a "mutual protective effect" between NiO and doping metal oxide, which inhibits the growth of particle size during the crystallization process.[7a]

For the Ni-Ti-O samples, only the characteristic peaks related to NiO structure are observable when the Ti content is 15% and below. An additional peak at 2θ around 25.1° appears in the sample with Ti loading of 20%. This peak can be indexed to the (101) plane of anatase TiO_2(JCPDS 21-7212),[18] which suggests the anatase TiO_2 phase is formed in the Ni-Ti mixed oxide sample with high Ti content. However, the SnO_2 phase is detectable in all the Ni-Sn-O

samples. Three weak peaks at 2θ about 26.0°, 33.4° and 51.1° are visible even in the lowest Sn loading sample of $Ni_{97.5}Sn_{2.5}$ oxide. These three peaks are ascribed to the (110), (101) and (211) planes in tetragonal phase of SnO_2 (JCPDS 41-1445).[19] In the case of Ni-W-O samples, additional peaks at 2θ of 23.4° and 33.5° being to emerge in the sample of $Ni_{95}W_{05}$ from the monoclinic WO_3 (JCPDS 43-1035) structure.[20] With increasing W concentration, these peaks become more evident.

On the basis of XRD results, the NiO crystal is the dominant phase in all the samples. Apart from this main phase, the structure related to the doping of the metal oxide begins to appear when the doping metal content increases to a certain level. In the case of Ti, the absence of observable TiO_2 phase in samples below 15% Ti leads us to hypothesize that most of the Ti atoms are incorporated into the NiO crystal structure. By contrast, the diffraction peaks ascribed to SnO_2 or WO_3 crystal structures are observed even with low Sn (2.5%) or W (5%) loading. From the XRD data, we're unable to determine whether some Sn or W is inserted into the NiO crystal lattice. Highly sensitive electron microscopy techniques will be used to probe for incorporation of dopants into the NiO crystal lattice.

The small particle sizes for the mixed oxides fit well with the high surface areas measured from the N_2 adsorption test (Figure 4). The surface area of these mixed oxide samples are in the range of 100 to 250 m^2/g, which are much higher than that of pure NiO (48 m^2/g). The unexpectedly high surface area of doped samples could be due to the presence of an amorphous layer of the doping metal oxide, as we suggested for Ni-Nb-O.[7c] It is noted that the surface area decreases in the samples with high dopant content, especially in sample $Ni_{80}W_{20}$ and $Ni_{80}Sn_{20}$. This could be due to the formation of separate phases of WO_3 and SnO_2, and they have higher density than NiO. These mixed oxide materials have smaller particle size and bigger surface area than those

made using the typical evaporation method,[8a, 10, 21] which indicates the advantage of this "***dry mixing***" synthesis for obtaining nano-structured materials.

Recent results suggest that the ethane ODH reaction over the NiO based catalyst takes place via a Mars-van Krevelen (MVK) mechanism, with the participation of lattice oxygen.[22] In the MVK mechanism, a redox process occurring on the surface of NiO catalyst, is an important step for sustaining the catalytic cycle. Thus, the reduction property of NiO is an important parameter for understanding catalyst performance. H_2-TPR was performed on the selected Ni-Ti-O, Ni-Sn-O and Ni-W-O samples. In all the samples (Figure 5, 6 and 7), a small peak located at 210 °C is clearly visible. A peak at this same position was reported by Nieto et al in NiO-CeO_2 mixed oxides, which they attributed to the reduction of adsorbed oxygen species on the CeO_2 surface.[23] In our case, all the samples demonstrated this peak at the same position, which is unaffected from changing the doping metal. Thus, we conclude that this peak is derived from the phase relevant to NiO structure (pure NiO or M-Ni-O solid solution) rather than the doping metal oxides. This conclusion is consistent with the report of non-stoichiometric oxygen on an NiO surface, which confirmed that the weak peak at around 200 °C is due to the reduction of nonstoichiometric electrophilic oxygen $O^{\bullet -}$ species.[24] Such oxygen species is believed to be associated directly with the first C-H bond activation of ethane but is inversely correlated to ethylene selectivity.[22] This peak is hardly observed in Nb and Ta doped as well as undoped NiO catalysts prepared using the sol-gel method.[7c, 9] Therefore, the concentration of electrophilic oxygen $O^{\bullet -}$ species in NiO based materials made using the dry mixing method is much higher than that sol-gel prepared samples, which could explain their different catalytic performance. Moreover, the intensity of the peak related to non-stoichiometric electrophilic oxygen decreases

with the increase of doping metal loading. Particularly, this peak almost disappears in the samples of $Ni_{0.80}Ti_{0.20}$ and $Ni_{0.80}W_{0.20}$ oxide. These phenomena prove that doping NiO with a secondary metal could reduce the over-stoichiometric oxygen and thus, change the catalytic performance.

Besides the small peak for non-stoichiometric electrophilic oxygen, additional peaks above 260 °C are relevant to the reduction of NiO and the dopant metal oxide. As for the pure NiO, the reduction peak is located at around 290 °C with a shoulder at about 320 °C.[8a, 10] The peak for NiO reduction shifts to higher temperatures in all the doped samples. The NiO reduction temperature is dependent on the nature of the dopant. The reduction temperature of our M-NiO materials follows a sequence of Ni-Ti-O > Ni-W-O > Ni-Sn-O. The difference in reduction temperature among these three kinds of catalysts could be ascribed to the different interactions between NiO and these doping metal oxides. Also, the reduction peak shifts to high temperature when the content of Ti or W increases in the mixed oxide. However, the NiO reduction temperature is not affected by the Sn content, which is similar to previous observations.[10]

In the samples of Ni-Sn-O and Ni-Ti-O, only the peak related to the reduction of NiO is detectable. As suggested by XPS characterization below, the Ti exists as Ti^{4+}, while the Sn exists as Sn^{2+} and Sn^{4+}. It should be mentioned that the reduction of bulk oxygen in tin (II, IV) and Ti (IV) has been confirmed to occur at around 600 °C and 650 °C, respectively.[10, 25] However, the peaks resulting from the reduction of Ti^{4+}, Sn^{4+} and Sn^{2+} species are not detectable in these two types of samples, indicating that the Sn and Ti species becomes less reducible when they are doped into NiO. By contrast, a peak at 750 °C due to the reduction of W species is observed in the $Ni_{0.85}W_{0.15}$ and $Ni_{0.80}W_{0.20}$ samples,[8a] further confirming the existence of WO_3 phase in the mixed oxide.

The XPS characterization was further used to identify the chemical state of the selected NiO samples with 5% and 10% doping metal loading. Figure 8 shows the high resolution XPS spectra of the Ni 2p core level from the different doped nickel samples of Ni-W-O, Ni-Sn-O, and Ni-Ti-O. A full understanding of the Ni XPS spectrum still remains a matter of debate due to the controversy in the interpretation of spectrum.[26] The analysis of our spectra was based on the fitting method from a reference, and a Shirley background was applied across the $Ni2p_{3/2}$ portion of the spectra.[27] The spectrum Ni $2p_{3/2}$ nickel portion is well fitted with a combination of spectra obtained from standard NiO, $Ni(OH)_2$, and NiOOH samples, and the concentration of each species is listed in Table S1. It should be noted that the NiO is the dominant state in all the samples, which is consistent with the observation from XRD characterization. The presence of $Ni(OH)_2$ could arise from the hydration of surface NiO. The presence of Ni^{3+} species indicates there is non-stoichiometric structure in the NiO structure. The h^+ could be localized on Ni^{2+} site to form Ni^{3+} ($Ni^{2+} + h^+ \rightarrow Ni^{3+}$), and this non-stoichiometric structure results in a low reduction peak at around 200 °C as observed in the TPR spectra described above. The concentration of Ni^{3+} species arising from NiOOH decreases with an increase of doping metal content, suggesting that doping metal into NiO could reduce non-stoichiometric structure in NiO.

Figure 9 shows the high resolution XPS spectra of the W 4f core level from $Ni_{0.95}W_{0.05}$ and $Ni_{0.90}W_{0.10}$ samples. The W 4f core level was deconvoluted with one doublet W $4f_{7/2}$ – W $4f_{5/2}$ with a fixed area ratio equal to 4:3 and doublet separation of 2.15 eV. The binding energy of the $W4f_{7/2}$ component at 35.7 eV corresponds to W^{6+} in WO_3.[28] This XPS result verifies the presence of WO_3 in the Ni-W-O samples, which we observed via XRD analysis.

Figure 10 shows the high resolution XPS spectra of the Sn 3d core level from the nickel oxide doped with 5% and 10% Sn. The Sn $3d_{5/2}$ peak was fitted using three components located at

484.9, 486.3, and 487.0 eV, which are attributed to Sn^0 metallic tin, Sn^{2+} in SnO and Sn^{4+} in SnO_2, respectively.[29] The tin(IV) acetate is the Sn precursor for the preparation of Ni-Sn-O samples. However, most of Sn^{4+} in tin (IV) acetate gets reduced by the oxalic acid during the synthesis process, resulting in the formation of Sn^{2+} and Sn^0 in the mixed oxide. The existence of Sn^{4+} as SnO_2 was observed in our XRD analyses described previously. However, the presence of Sn^{2+} as an independent bulk structure had not yet been observed, so the Sn^{2+} could exist as small clusters or in the NiO crystalline structure. Note the amount of Sn^0 observed through XPS is negligible, and therefore it is not detected by other techniques.

Figure 11 shows high resolution XPS spectra of the Ti 2p core level from $Ni_{0.95}Ti_{0.05}$ and $Ni_{0.90}Ti_{0.10}$. The Ti $2p_{3/2}$ peak was fitted using one component located at 458.4 eV corresponding to TiO_2. This observation is in agreement with our findings from XRD characterization.[30]

The SEM images of the Ti, Sn and W doped NiO materials are shown in the supplementary information (Figure S1**)**. The images show the NiO based materials possess similar morphology. The primary particles are not uniform; and the sizes range from 1 to 4 μm.

More detailed morphology information of these NiO based materials was obtained by BF-TEM and HAADF-STEM techniques. BF-TEM revealed that the big particles (> 1 μm) seen in SEM micrographs are not single crystallites, but are aggregates of small particles measuring 1-5 nanometers (Figure 12). The selected area electron diffraction (SAED) characterization was applied to these areas for the further probe of the structure of the mixed oxides. These SAED patterns are shown as inserts in the each electron micrograph of Figure 12. It can be noticed from those SAEDs that all the samples have similar patterns of diffraction rings, indicating they possess identical structure. Furthermore, the observed diffraction rings match quite well with the

characteristic structure of cubic NiO phase. These diffraction patterns can be attributed to the (111), (200), (220), (311), (222), (400), (331) and (422) planes of cubic phase NiO, confirming the formation of well-crystalline feature of the NiO structure. SAED did not reveal the diffraction patterns diagnostic of crystalline SnO_2, TiO_2, and WO_3 which were clearly observed via XRD. However, TEM-EDS analysis (Figure S2) on these three samples clearly reveals the presence of Ti, Sn and Win the mixed oxides. The Ti, Sn and W exist as small oxide clusters or are incorporated into the NiO crystalline structure, which makes them difficult detect by electron diffraction.

In order to further investigate the dispersion of doping metals into NiO at the atomic level, high angle annular dark field (HAADF) STEM imaging analysis was performed. It is equipped with an aberration corrector to reduce the spherical aberration so that STEM micrographs contain a sub-Å spatial resolution. The aberration corrector improves single atom sensitivity and visibility in the acquired micrograph, which has been successfully used in identification of single atom catalyst.[31] As revealed in a previous report by Wachs *et al*,[31d] individual W atoms and small WO_3 clusters are clearly resolved by HAADF-STEM in the WO_3/ZrO_2 catalyst. Regarding the $Ni_{0.90}W_{0.10}$ catalysts, the W atoms should be in principle observable in HAADF-STEM, because of a large Z contrast difference arising from different atomic number of W and Ni. In the HAADF-STEM images small particles approximately 2-4 nm in diameter are clearly observable, which possess the characteristic NiO like strucuture (Figure 13). EDS analysis (Figure S3) on the area in Figure 13a shows the presence of both Ni and W elements, suggesting a intimate structure comprising Ni and W components was formed. The measured interplanar distance of 2.38 Å is consistent with the (111) plane of NiO. More importantly, there is an array of bright dots and spots highly dispersed in these small particles, which were never observable by

conventional TEM analysis. From the report by Wachs *et* al[31d] we conclude that these bright dots are attributed to individual tungsten atoms. Indeed, two different kinds of tungsten arrangements are distinguishable in the mixed oxide, which are highlighted by yellow and red circles in Figure 13c. The bright dots in the yellow circles correspond to isolated tungsten atoms. These atoms are present inside the NiO crystal lattice forming the solid solution. Those spots in red circles should be WO_3 clusters (or small particles). Further EDS analysis (Figure S4) on a circle indicates high concentration of W in this area, thus confirming it is poly-tungstate species at the surface of NiO. This observation is also consistent with the XRD and H_2-TPR characterizations results, which already suggested that there is a separate WO_3 phase in the mixed oxide. On the basis of HAADF in STEM, we can conclude that there are two kinds of tungsten structures in the mixed oxide. The major portion of the tungsten atoms are incorporated into the NiO structure for the formation of the Ni-W-O solid solution and a small amount of WO_3 clusters are located at the surface of the NiO particles. It should be noted that this is a typical example of using the HAADF STEM technique to study the doped NiO based catalysts, and the result here provide a direct and strong proof that transition metals are incorporated into the NiO crystal lattice.

In the case of our $Ni_{0.90}Ti_{0.10}$ and $Ni_{0.90}Sn_{0.90}$ samples, the Ti and Sn atoms are not as clearly resolved as the W atoms in HAADF micrographs. In STEM, the resolution is highly dependent on the ability of a target atom to scatter the electron beam. Heavier atoms are more easily visualized, because the higher atomic mass results in stronger electron scattering. The atomic number between Ni and Ti or Sn is close, and therefore the Ti and Sn atoms located at NiO matrix cannot be well identified. (Figure S5 and S6). We can however still find some bright dots and spots which appear to be the doping metal atoms at the surface of NiO.

4.2. Structural stabiltiy of doped NiO from DFT calculations

The characterization results described above indicated that it is possible to incorporate the doping metal atoms into the NiO crystalline structure. In this section, we will discuss the thermodynamic feasibility of assembling the mixed metal oxide materials from individual elements using DFT calculations based on their computed formation energy following the formalisms described in section 3.2. Figure 1 illustrates the DFT-optimized crystal structures of the M-doped NiO materials (M = Ti, Sn and W) explored in our calculations with 3 atom % of dopant (atomic concentration in the range of the obtained experimental data).

Considering first the pure NiO, the calculated formation energy for the perfect structure is found to be -74.5 KJ/mol, while that for the defective structure $Ni_{0.96}O$ associated to two extra holes is found to be -87.4 KJ/mol (Figure S7). As the formation energy of $Ni_{0.96}O$ is lower than that of the perfect one, it can be concluded that the defective structure in NiO is thermodynamically more favorable than the perfect one. Our computational results are supported by the fact that NiO is found as a non-stoichiometric material with defects in its structure, and this crystallographic defect is the origin of the *p*-type conductive property of this material.[32] Since the non-stoichiometric nickle oxide structure with a composion of $Ni_{0.96}O$ is more stable than the pure NiO, it will be used as our initial structure for establishing the structure of doped NiO.

The computed formation energies of the structures of $Ni_{0.93}Ti_{0.03}$ (neutral system) and $Ni_{0.90}Ti_{0.03}$ (with two extra holes) associated to created Ti^{4+} ions are found to be -104.2 KJ/mol and -106.8 KJ/mol, respectively (Figure S8). Comparing with $Ni_{0.96}O$, we can clearly see that both configurations have lower formation energy, and so, these two compounds are likely to be thermodynamically more stable than $Ni_{0.96}O$.

We also calculated the formation energies of $Ni_{0.93}Sn_{0.03}O$ (neutral system) and $Ni_{0.90}Sn_{0.03}O$ (two extra holes) structures with created Sn^{4+} ions and values of -91.1 KJ/mol and -94.6 KJ/mol were obtained, respectively (Figure S9). Both values are slightly lower than that for $Ni_{0.96}O$, which means that these two compounds are likely to be more favorable than $Ni_{0.96}O$. In contrast, the $Ni_{0.96}Sn_{0.03}O$ structure (neutral system) associated to created Sn^{2+} ions has given a formation energy of -82.8 KJ/mol, which is higher than that obtained for $Ni_{0.96}O$ (Figure S10). This results means that the $Ni_{0.96}Sn_{0.03}O$ material is likely to be less favourable than $Ni_{0.96}O$.

For W-doped NiO compounds, our computed formation energies of $Ni_{0.90}W_{0.03}O$ (neutral system) and $Ni_{0.87}W_{0.03}O$ (with two extra holes) structures associated to W^{6+} ions are found to be -99.0 KJ/mol and -108.7 KJ/mol, respectively (Figure S11). As these two values are clearly lower than that obtained for $Ni_{0.96}O$, it can be understood that both structures are likely to be thermodynamically more stable than $Ni_{0.96}O$.

As discussed above, the DFT calculation results proved that the incorporation of metal dopant into NiO is a thermodynamically favorable process. NiO doped with Ti, Sn and W are found to be more stable than the pure NiO and the non-stoichiometric $Ni_{0.96}O$. The doping metals can occupy the Ni crystallographic site, and are incorporated into the crystalline structure of NiO, resulting in the formation of a new type of solid solution. Moreover, the incorporation of doping metal into NiO leads to a decrease of the amount of holes (h^+) in the structure, which will result in significantly decreasing non-stoichiometric oxygen in the NiO structure. The low concentration of non-stoichiometric oxygen in the doped NiO is the main reason for improving the cataltyic performance in ethane ODH.

4.3 Catalytic reaction

These three series of NiO based catalysts were tested in the oxidative dehydrogenation of ethane from 200 to 400 °C. As shown in our previous studies, only ethylene and carbon dioxide were detected as the reaction products in the ethane ODH reaction over the NiO based catalysts.[7c, 9] The absence of carbon monoxide as a by-product may be due to the oxidation of CO into CO_2 by NiO.[33]

These NiO catalysts were prepared by calcination at 300 ºC, and the catalytic reaction however was performed up to 400 ºC. A sintering of catalyst may happen when the reaction temperature exceeds 300 ºC, which could lead to a decrease of the activity. In order to clarify this doubt, a light-off behavior of one typical fresh catalyst $Ni_{0.90}Ti_{0.10}$ in ethane ODH was studied in a reaction cycle. The reaction cycle consists in one heating step (ramps at 1 ºC/minute from 250 to 350 ºC) followed by one cooling step (ramps at 1 ºC/minute from 350 to 250 ºC). Reaction result in Figure S12 shows that ethane conversion in cooling curve is almost similar to that in heating curve, which proves that no activity was lost when the catalyst was used above 300 ºC. The spent catalyst was further studied by TEM and nitrogen adsorption techniques. As shown in Figure S13, no evident sintering is observed and the particle size remains unchanged after the reaction. Moreover, the BET surface areas of the fresh (217 cm^2/g) and spent (210 cm^2/g) sample are quite similar. On a basis of these results, it can be concluded that catalysts prepared by calcination at 300 ºC reach a thermodynamically stable state, and their structure does not change when they are used in the reaction above 300 ºC.

Figure 14, 15 and 16 show the ethane conversion and ethylene selectivity over our NiO based catalysts, and the oxygen conversions are present in Figure S14, S15 and S16. It should be noted that ethane conversions reach a plateau accompanied with a slight increase of ethylene selectivity in most of catalysts, which is due to a large consumption of O_2 in the reaction. A general

tendency is observed that the addition of secondary metal by grinding method changes the activity of NiO in ethane ODH, which could be a result of the alteration of properties of NiO by the doping metals. Compared with pure NiO catalyst, almost all of the catalysts in the Ni-Ti-O and Ni-Sn-O families delivered higher conversion and all of them were more selective to ethylene. The enhanced activity may be due to the higher surface area and smaller particle size of these mixed oxides. However, in the Ni-W-O catalyst family only $Ni_{0.975}W_{0.025}$ exhibits a higher conversion than pure NiO with all of the samples exhibiting higher ethylene selectivity. This could be mainly due to the presense of non-stoichiometric oxygen observed by TPR at 200 °C decreasing in Ni-W-O oxides with increasing tungsten loading. As shown in Figure 7, the reduction peak for non-stoichiometric oxygen is a slight rise in the baseline for $Ni_{0.85}W_{0.15}$ and totally disappears in $Ni_{0.80}W_{0.20}$.

The selectivity is significantly improved by the doping of NiO with Sn, Ti, or W. In the reference sample of pure NiO, the selectivity is lower than 50% in all the temperatures investigated. The addition of a small amount of metal dopant (2.5%) into NiO results in enhancing the selectivity dramatically. Tungsten is observed to be the most efficient dopant for improving the selectivity. The incorporation of 2.5% W into NiO increases the selectivity to 65%. This dramatic selectivity increase from a small amount of added W is due to its strong ability to reduce the number of non-stoichiometric oxygen sites.

The over-oxidation of ethane into CO_2 is ascribed to excess non-stoichiometric oxygen at the surface of NiO catalyst. The non-stoichiometric oxygen is evidenced from the H_2-TPR peak at 200 °C, and it systematically decreases with increasing doping metal loading. Therefore, higher ethylene selectivity is achieved in the sample with higher doping.

The selectivity is related not only to the reaction temperature, but also to the ethane conversion. The study of ethylene selectivity versus ethane conversion was carried out by changing the contact time to get different levels of conversion and selectivity. The relationship between ethylene selectivity and ethane conversion at 330 °C grouped by metal dopant is shown in Figures 17, 18 and 19. The ethylene selectivity at the same level of ethane conversion is dependent on the doping metal loading. High metal oxide doping is beneficial for achieving improved selectivity. More importantly, the ethylene selectivity keeps almost stable with the increase of ethane conversion in all the catalysts, which suggests parallel reaction pathways for ethylene and CO_2 formation. That selectivity remains unchanged by contact time variation leads us to conclude that CO_2 is mainly produced by an over oxidation of ethane, and not by the secondary reaction of ethylene. The stability of ethylene at the surface of NiO is due to the difficulty of breaking the C=C of ethylene[34].

Two representative catalysts $Ni_{0.90}Ti_{0.10}$ and $Ni_{0.90}Sn_{0.10}$ were investigated in the stability test for 24 hours at 330 °C with a feed of 10% C_2H_6 and 5% O_2. The catalytic performances of these two catalysts over 24 hours of time-on-stream are presented in Figure S17 and S18. No evident loss of activity was observed and ethylene selectivity was well maintained in the reaction. These results are consistent with the findings in references[7-10], which proves that NiO based material is a stable catalyst for ethane ODH.

4.4 Discussion on structure-activity relationship in NiO based catalyst

The reaction mechanism of ethane ODH over NiO based catalyst has been studied by several groups.[7b, 22a, 35] All of these papers concluded that the electrophilic $O^{\bullet-}$ species, sometimes called O^-, at the NiO surface plays an important role in the ethane ODH reaction. The $O^{\bullet-}$ species is

believed to be formed via the electron exchange between the lattice O^{2-} and positive h^{+} originated from the p-doping of NiO.[7a] Then, the abundance of nickel vacancies in the pure NiO leads to the formation of a high concentration of $O^{\bullet-}$ species at the NiO surface. Recently, using a direct kinetic isotope study, it was proposed that the $O^{\bullet-}$ species is responsible for activating the C-H bond, leading to a homolytic scission of C-H bond that is the rate determining step in the ethane ODH reaction (a kinetic isotope effect was observed between C_2H_6 and C_2D_6).[22a] The $O^{\bullet-}$ species attacking a C-H bond in ethane results in the abstraction of $H^{\bullet}$ from ethane, which forms an ethyl radical at the "surface" of NiO. It is not fully understood where this ethyl radical coordinates to the surface: it could be bonded to a Ni^{2+} or an O^{2-} site which are equally abundant on the surface. On a semi-conductor it will find enough electrons in the conduction band to couple with one of these electrons without looking for localized bonding. We assume that it will coordinate to the "surface" as a coordinated ethyl without specifying the coordination site. This surface ethyl radical would lead to ethylene by beta-H elimination or it can react further the $O^{\bullet-}$ to give CO_2 (Scheme 1).

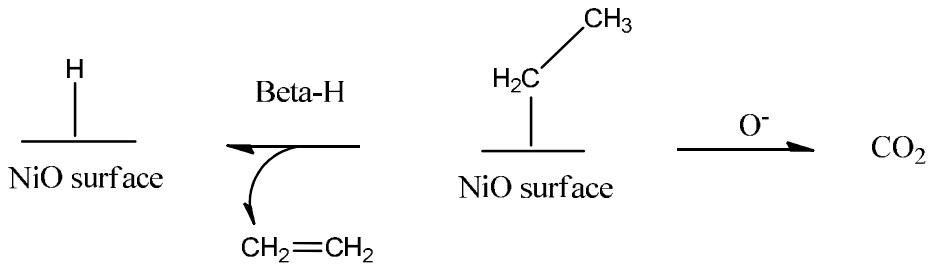

Scheme 1 Ethyl group transformation at the surface of NiO based catalyst.

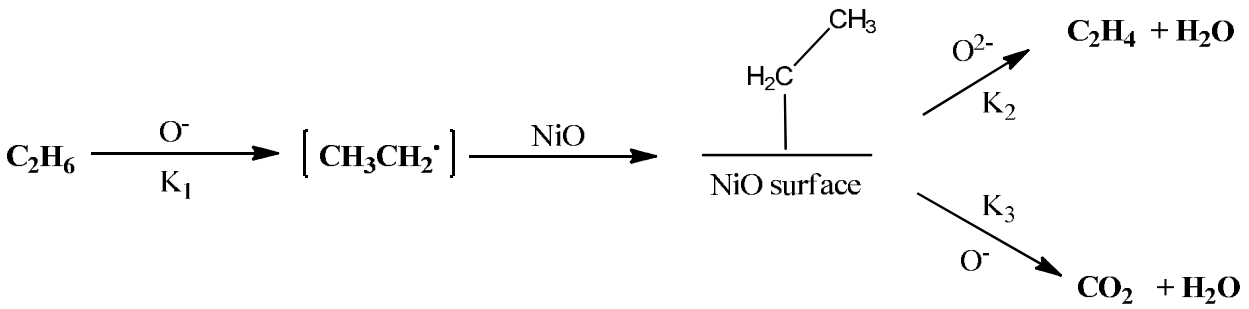

Scheme 2 Summarized reaction pathway of ethane ODH over NiO based catalysts from references.[7a, 23] We have purposely not precisely identified whether the ethyl radical is linked to surface oxygen or nickel atoms due to a lack of experimental and theoretical evidence.

It is clear that the high concentration of $O^{\bullet-}$ species, generated by the presence of holes leads to increased formation of CO_2 in undoped NiO. Therefore, this electrophilic oxygen $O^{\bullet-}$ is likely responsible for the formation of CO_2 from a surface bond ethyl group.[22a] On the basis of this understanding, a reaction pathway for ethane ODH over NiO can be generalized in Scheme 2. In this simplified reaction pathway, K_1 and K_3 are linked to the concentration of $O^{\bullet-}$ species at the NiO surface as confirmed by several groups.[26] K_2 is presumably correlated with the reactivity of lattice O^{2-},[36] which can be evaluated from the H_2-TPR test. The low reduction temperature in H_2-TPR indicates a high reactivity of the lattice oxygen toward the β-hydrogen elimination, and as a result the high K_2 value for ethylene formation is obtained. Overall, the ethane conversion and ethylene selectivity can be therefore correlated to K_1, K_2 and K_3. The ethane conversion is dependent only on K_1, since the C-H bond cleavage is the rate determining step, whereas the ethylene selectivity is dependent upon K_2/K_3.

Based on the important conclusions discussed above, the key point for the design of highly efficient NiO catalysts for ethane ODH is rational control of non-stoichiometric oxygen at the surface of NiO. The concentration of $O^{\bullet-}$ species at the surface of NiO needs to be controlled carefully to a reasonable level. Too much $O^{\bullet-}$ at the surface of NiO will ultimately lead to a total

oxidation of ethane into CO_2 (K_3>>K_2). On the contrary, a low concentration of $O^{\bullet-}$ will result in severely limit its ability to activate ethane at low temperature (K_1 close to 0). Therefore, the concentration of non-stoichiometric oxygen should be precisely balanced to merely activate ethane for its transformation at the surface of NiO, but does not lead to it completely burning into CO_2 (K_1>0, and K_2>> K_3). NiO is intrinsically active for ethane oxidation at relatively low temperature, but it is not selective for the formation of ethylene due to high concentration of non-stoichiometric oxygen in its structure. It is proven that transition metal doped into NiO could largely reduce the non-stoichiometric oxygen concentration in NiO due to a significant decrease of positive h^+, resulting in a dramatic increase of ethylene selectivity in ethane ODH. We found that the catalyst preparation method has also significant effect on the structure and property of NiO bringing about different catalytic behavior in the ethane ODH.[7c, 9] Accordingly, we have developed a simple but efficient dry grinding method for the synthesis of Ni-Nb-O catalysts.[11] In this report we attempted to extend this preparation method to other NiO based catalysts, and fortunately it is applicable for synthesizing Ni-Sn-O, Ni-Ti-O and Ni-W-O catalysts. Characterization techniques and DFT calculation cleanly indicate that these doping metals were inserted into the NiO structure, forming a solid solution between NiO and the secondary metal oxide.

These three series of Ni-Sn-O, Ni-Ti-O and Ni-W-O catalysts (Ni-Sn-O, Ni-Ti-O and Ni-W-O) exhibit enhanced efficiency in ethane ODH reaction as compared with pure NiO, which is mainly due to the modification of NiO structure by doping metals. Doping NiO with Sn, Ti or W has three effects on the nature of the NiO, all of which affect the catalyst performance. Firstly, the concentration of non-stoichiometric oxygen in the mixed oxides largely reduces owing to the decrease of the amount of holes (h^+) in the structure, and the amount of non-stoichiometric

oxygen is inversely associated with the doping metal loading as indicated from H_2-TPR characterization. The decrease of $O^{\bullet-}$ species in NiO brings about two consequences: (1) the selectivity to ethylene is largely improved due to the decrease of K_3; (2) the ethane conversion decreases is some cases especially the Ni-W-O series, because K_1 becomes smaller. Secondly, the particle size of NiO significantly decreases accompanied with an increase of surface area. The reduced particle size is due to the formation of a protective layer (such as SnO_2, TiO_2 or WO_3 clusters) around NiO surface stabilizing small NiO particles. Smaller NiO particles results in a higher number and enhanced access to active sites increasing ethane conversion. It is found that the decrease of active oxygen species ($O^{\bullet-}$) does not lead to a significant loss of activity in the Ni-Ti-O and Ni-Sn-O catalysts as compared with pure NiO, because the loss of active oxygen ($O^{\bullet-}$) is compensated by the increased accessibility to the active sites. Lastly, the mixed oxides exhibit less reducibility than the pure NiO due to the strong interaction between the doping meal oxide and NiO. This phenomenon should in principle reduce the ethylene selectivity because of the decrease of K_2. However, such hypothesis was never confirmed in the catalysts studied. In fact, the decrease of K_3 is much faster than that of K_2 because of significant loss of $O^{\bullet-}$; therefore the ethylene selectivity still increases to a high level. Taking these three aspects into consideration together, increased ethylene production is indeed achieved by these doped NiO catalysts synthesized with our solid grinding method.

5. Conclusions

The solid state grinding synthesis method previously disclosed for Ni-Nb-O and Ni-Ta-O mixed oxides was successfully extended to three series of Ni-Sn-O, Ni-Ti-O and Ni-W-O catalysts with

different levels of dopants. Characterization techniques including XRD, N_2 adsorption, H_2-TPR, XSP, bright filed SEM and high angle annular dark field (HAADF) STEM were used to study the detailed structure and properties of these catalysts. The structure of the mixed oxides has a certain level of heterogeneity, which is mainly composed of two phases: Ni_xM_yO (M = Sn, Ti or W) solid solution (NiO crystalline structure with doping atom in the lattice) and secondary metal oxide (SnO_2, TiO_2 or WO_3). DFT calculations performed on the formation energies of solid Ni-M-O solution structures clearly confirmed the thermodynamic feasiblility of incoporating these doping metals into the NiO structure. NiO doped with Sn, Ti and W were found to be more stable than the pure NiO and the non-stoichiometric $Ni_{0.96}O$. The incorporation of doping metals into NiO significantly decreases the particle size to around 4 nm and increases the surface area up to 250 m^2/g. The presence of non-stoichiometric oxygen was confirmed in the H_2-TPR test, and it dramatically decreases with dopant content because of less holes (h^+) in the doped NiO. The mixed oxides become less reducible due to the strong interaction between NiO and doping metal oxide.

These catalysts exhibit high performance for the production of ethylene from ethane oxidative dehydrogenation reaction. The enhanced performance is mainly due to a significant elimination of non-stoichiometric oxygen and decrease of particle size opening up more active sites. The low concentration of non-stoichiometric oxygen in the mixed oxide suppresses the formation of CO_2 byproduct, resulting in dramatilly increasing the ethylene selectivity. The reduced particle size and increased surface area compensate the loss of actvity arising from the low $O^{\bullet-}$ content and therefore, the activity of mixed oxide is still kept at a relatively high level. As a consequence of these two facts, the high ethylene production efficiency was achieved in the mixed oxide catalysts.

Supporting Information.

These include SEM images of Ni-Sn-O, Ni-Ti-O and Ni-W-O samples, EDS in TEM analysis on Ni-Sn-O, Ni-Ti-O and Ni-W-O catalysts, HAADF STEM images from $Ni_{0.90}Ti_{0.10}$ and $Ni_{0.90}Sn_{0.10}$ oxides and formation energies of M-doped NiO structures (M = Sn, Ti and W). This material is available free of charge via the Internet at http://pubs.acs.org.

AUTHOR INFORMATION

Corresponding Author

* E-mail: jeanmarie.basset@kaust.edu.sa

Acknowledgment

The authors acknowledge financial support from The Dow Chemical Company.

REFERENCES

(1) True, W. R. *Oil Gas J.* **2010**, *108*, 34-38.
(2) Ren, T.; Patel, M.; Blok, K. *Energy* **2006**, *31*, 425-451.
(3) (a) Gärtner, C. A.; van Veen, A. C.; Lercher, J. A. *ChemCatChem* **2013**, *5*, 3196-3217;(b) Valente, J. S.; Armendáriz-Herrera, H.; Quintana-Solórzano, R.; del Ángel, P.; Nava, N.; Massó, A.; López Nieto, J. M. *ACS Catalysis* **2014**, *4*, 1292-1301; (c) Zhu, H.; Laveille, P.; Rosenfeld, D. C.; Hedhili, M. N.; Basset, J.-M. *Catal. Sci. Technol.* **2015**, *5,* 4164-4173 (d) Koirala, R.; Buechel, R.; Krumeich, F.; Pratsinis, S. E.; Baiker, A. *ACS Catalysis* **2015**, *5*, 690-702.
(4) Cavani, F.; Ballarini, N.; Cericola, A. *Catal. Today* **2007**, *127*, 113-131.
(5) Bhasin, M. M. *Top. Catal.* **2003**, *23*, 145-149.
(6) (a) Seshan, K. In *Catalysis: Volume 22*, The Royal Society of Chemistry: 2010; Vol. 22, pp 119-143;(b) Nieto, J. M. L.; Solsona, B.; Grasselli, R. K.; Concepcion, P. *Top. Catal.* **2014**, *57*, 1248-1255;(c) Popescu, I.; Heracleous, E.; Skoufa, Z.; Lemonidou, A.; Marcu, I.-C. *Phys. Chem. Chem. Phys.* **2014,** *16*, 4962-4970;(d) Qin, Z.; Zhou, D. S.; Wu, Y.; Wu, T. H. *J. Rare Earths* **2013**, *31*, 669-673.
(7) (a) Savova, B.; Loridant, S.; Filkova, D.; Millet, J. M. M. *Appl. Catal., A* **2010**, *390*, 148-157;(b) Skoufa, Z.; Heracleous, E.; Lemonidou, A. A. *Catal. Today* **2012**, *192*, 169-176;(c) Zhu, H.; Ould-Chikh, S.; Anjum, D. H.; Sun, M.; Biausque, G.; Basset, J.-M.; Caps, V. *J. Catal.* **2012**,

285, 292-303;(d) Skoufa, Z.; Heracleous, E.; Lemonidou, A. A. *Chem. Eng. Sci.* **2012**, *84*, 48-56;(e) Santander, J.; Lopez, E.; Diez, A.; Dennehy, M.; Pedernera, M.; Tonetto, G. *Chem. Eng. J.* **2014**, *255*, 185-194; (f) Zhu, H.; Rosenfeld, D. C.; Anjum, D. H.; Sangaru, S. S.; Saih, Y.; Ould-Chikh, S.; Basset, J.-M. *J. Catal.* **2015**, *329*, 291-306.
(8) (a) Solsona, B.; López Nieto, J. M.; Concepción, P.; Dejoz, A.; Ivars, F.; Vázquez, M. I. *J. Catal.* **2011**, *280*, 28-39;(b) Agouram, S.; Dejoz, A.; Ivars, F.; Vazquez, I.; Nieto, J. M. L.; Solsona, B. *Fuel Process. Technol.* **2014**, *119*, 105-113.
(9) Zhu, H.; Dong, H.; Laveille, P.; Saih, Y.; Caps, V.; Basset, J.-M. *Catal. Today* **2014**, *228*, 58-64.
(10) Solsona, B.; Concepción, P.; Demicol, B.; Hernández, S.; Delgado, J. J.; Calvino, J. J.; López Nieto, J. M. *J. Catal.* **2012**, *295*, 104-114.
(11) Zhu, H.; Rosenfeld, D. C.; Anjum, D. H.; Caps, V.; Basset, J.-M. *ChemSusChem* **2015**, *8*, 1254-1263.
(12) (a) Kresse, G.; Hafner, J. *Phys. Rev. B* **1994**, *49*, 14251-14269; (b) Kresse, G.; Furthmüller, J. *Phys. Rev. B* **1996**, *54*, 11169-11186; (c) Kresse, G.; Furthmüller, J. *Comput. Mater. Sci*. **1996**, *6*, 15-50; (d) Kresse, G.; Joubert, D. *Phys. Rev. B* **1999**, *59*, 1758-1775.
(13) Perdew, J. P.; Burke, K.; Ernzerhof, M. *Phys. Rev. Lett.* **1996,** *77*, 3865-3868.
(14) Blöchl, P. E. *Phys. Rev. B* **1994**, *50*, 17953-17979.
(15) Monkhorst, H. J.; Pack, J. D. *Phys. Rev. B* **1976**, *13*, 5188-5192.
(16) Hoffmann, M. R.; Martin, S. T.; Choi, W.; Bahnemann, D. W. *Chem. Rev.***1995**, *95*, 69-96.
(17) Delley, B. *J. Chem. Phys.* **1990**, *92*, 508-517.
(18) Sun, F.; Zhou, W.; Tian, G.; Pan, K.; Miao, X.; Li, Y.; Zhang, G.; Li, T.; Fu, H. *ChemCatChem* **2012**, *4*, 844-850.
(19) Bellayer, S.; Viau, L.; Tebby, Z.; Toupance, T.; Bideau, J. L.; Vioux, A. *Dalton Trans.* **2009**, 1307-1313.
(20) Kalanur, S. S.; Hwang, Y. J.; Chae, S. Y.; Joo, O. S. *J. Mater. Chem. A* **2013**, *1*, 3479-3488.
(21) Agouram, S.; Dejoz, A.; Ivars, F.; Vázquez, I.; López Nieto, J. M.; Solsona, B. *Fuel Process. Technol.* **2014**, *119*, 105-113.
(22) (a) Skoufa, Z.; Heracleous, E.; Lemonidou, A. A. *J. Catal.* **2015**, *322*, 118-129; (b) Heracleous, E.; Lemonidou, A. A. *J. Catal.* **2006**, *237*, 175-189.
(23) Solsona, B.; Concepción, P.; Hernández, S.; Demicol, B.; Nieto, J. M. L. *Catal. Today* **2012**, *180*, 51-58.
(24) Kotsev, N.; Ilieva, L. *Catal. Lett.* **1993**, *18*, 173-176.
(25) (a) de Resende, N. S.; Eon, J.-G.; Schmal, M. *J. Catal.***1999**, *183*, 6-13;(b) Xiaoyuan, J.; Guanghui, D.; Liping, L.; Yingxu, C.; Xiaoming, Z. *J. Mol. Catal. A: Chem.* **2004**, *218*, 187-195.
(26) (a) Alders, D.; Voogt, F. C.; Hibma, T.; Sawatzky, G. A. *Phys. Rev. B* **1996**, *54*, 7716-7719; (b) Biju, V.; Abdul Khadar, M. *J. Nanopart. Res.* **2002**, *4*, 247-253.
(27) Biesinger, M. C.; Payne, B. P.; Lau, L. W. M.; Gerson, A.; Smart, R. S. C. *Surf. Interface Anal.* **2009**, *41*, 324-332.
(28) Barreca, D.; Carta, G.; Gasparotto, A.; Rossetto, G.; Tondello, E.; Zanella, P. *Surf. Sci. Spectra* **2001**, *8*, 258-267.
(29) (a) Kövér, L.; Kovács, Z.; Sanjinés, R.; Moretti, G.; Cserny, I.; Margaritondo, G.; Pálinkás, J.; Adachi, H. *Surf. Interface Anal.***1995**, *23*, 461-466; (b) Quackenbush, N. F.; Allen, J. P.; Scanlon, D. O.; Sallis, S.; Hewlett, J. A.; Nandur, A. S.; Chen, B.; Smith, K. E.; Weiland, C.; Fischer, D. A.; Woicik, J. C.; White, B. E.; Watson, G. W.; Piper, L. F. J. *Chem. Mater.* **2013**,

25, 3114-3123; (c) Hanyš, P.; Janeček, P.; Matolı´n, V.; Korotcenkov, G.; Nehasil, V. *Surf. Sci.* **2006**, *600*, 4233-4238.
(30) Biesinger, M. C.; Lau, L. W. M.; Gerson, A. R.; Smart, R. S. C. *Appl. Surf. Sci.* **2010**, *257*, 887-898.
(31) (a) Qiao, B.; Wang, A.; Yang, X.; Allard, L. F.; Jiang, Z.; Cui, Y.; Liu, J.; Li, J.; Zhang, T. *Nat. Chem.* **2011**, *3*, 634-641;(b) Wang, S.; Borisevich, A. Y.; Rashkeev, S. N.; Glazoff, M. V.; Sohlberg, K.; Pennycook, S. J.; Pantelides, S. T. *Nat. Mater.* **2004**, *3*, 143-146;(c) Weckhuysen, B. M. *Nat. Chem.* **2009**, *1*, 690-692;(d) Zhou, W.; Ross-Medgaarden, E. I.; Knowles, W. V.; Wong, M. S.; Wachs, I. E.; Kiely, C. J. *Nat. Chem.* **2009**, *1*, 722-728.
(32) Huang, Z.; Natu, G.; Ji, Z.; He, M.; Yu, M.; Wu, Y. *J. Phys. Chem. C* **2012**, *116*, 26239-26246.
(33) Laveille, P.; Biausque, G.; Zhu, H.; Basset, J.-M.; Caps, V. *Catal. Today* **2013**, *203*, 3-9.
(34) Blanksby, S. J.; Ellison, G. B. *Acc. Chem. Res.***2003**, *36*, 255-263.
(35) (a) Skoufa, Z.; Xantri, G.; Heracleous, E.; Lemonidou, *Appl. Catal., A* **2014**, *471*, 107-117; (b) Sun, X. Y.; Li, B.; Metiu, H. *J. Phys. Chem. C* **2013**, *117*, 23597-23608; (c) Lin, X. F.; Xi, Y. Y.; Sun, J. *J. Phys. Chem. C* **2012**, *116*, 3503-3516.
(36) Centi, G.; Cavani, F.; Trifirò, F. *Selective Oxidation by Heterogeneous Catalysis*. Kluwer Academic/Plenum Publishers: New York **2001**.

Figure Captions

Figure 1. DFT-optimized structures for: (a) $Ni_{0.93}Ti_{0.03}O$ or $Ni_{0.93}Sn_{0.03}O$, (b) $Ni_{0.90}Ti_{0.03}O$ or $Ni_{0.90}Sn_{0.03}O$, (c) $Ni_{0.90}W_{0.03}O$, and (d) $Ni_{0.87}W_{0.03}O$. Color legend: Ni in dark blue, O in red, Ni vacancies in black, Ti or Sn in gray, W in light blue. The dopant elements are shown in big size balls.

Figure 2. X-ray diffraction patterns of Ni-Ti oxides (a), Ni-Sn oxides (b), and Ni-W oxides (c) with different loading.

Figure 3. Particle size of Ni-Sn-O, Ni-Ti-O and Ni-W-O catalysts with different dopant content.

Figure 4. Specific surface area of Ni-Sn-O, Ni-Ti-O and Ni-W-O catalysts with different dopant content.

Figure 5. H_2-TPR spectra of Ni-Ti oxides with different Ti loadings.

Figure 6. H_2-TPR spectra of Ni-Sn oxides with different Sn loadings.

Figure 7. H_2-TPR spectra of Ni-W oxides with different W loadings.

Figure 8. XPS spectra of the Ni 2p core level in the typical Ni-Sn, Ni-Ti and Ni-W mixed oxide samples.

Figure 9. High resolution XPS spectra of the W 4f core level from $Ni_{0.95}W_{0.05}$ and $Ni_{0.90}W_{0.10}$ oxide samples.

Figure 10. High resolution XPS spectra of the Sn 3d core level from $Ni_{0.95}Sn_{0.05}$ and $Ni_{0.90}Sn_{0.10}$ oxide samples.

Figure 11. High resolution XPS spectra of the Ti 2p core level from $Ni_{0.95}Ti_{0.05}$ and $Ni_{0.90}Ti_{0.10}$ oxide samples.

Figure 12. TEM images of $Ni_{0.90}Sn_{0.10}$, $Ni_{0.90}Ti_{0.10}$ and $Ni_{0.90}W_{0.10}$ samples, and corresponding electron diffraction.

Figure 13. HAADF images from a $Ni_{0.90}W_{0.10}$ oxide sample with different magnifications. Small crystals can be seen in Figure a (low magnification). Red circles in Figure b (high magnification) indicate WO_3 clusters located at the surface of NiO. Yellow circles in Figure c (high magnification) indicate the presence of single tungsten atoms corresponding to W incorporated into NiO lattice.

Figure 14. Ethane conversion (line) and ethylene selectivity (dotted line) over Ni-Ti-O catalysts.

Figure 15. Ethane conversion (line) and ethylene selectivity (dotted line) over Ni-Sn-O catalysts.

Figure 16. Ethane conversion (line) and ethylene selectivity (dotted line) over Ni-W-O catalysts.

Figure 17. Ethane conversion versus ethylene selectivity over Ni-Ti-O catalysts.

Figure 18. Ethane conversion versus ethylene selectivity over Ni-Sn-O catalysts.

Figure 19. Ethane conversion versus ethylene selectivity over Ni-W-O catalysts.

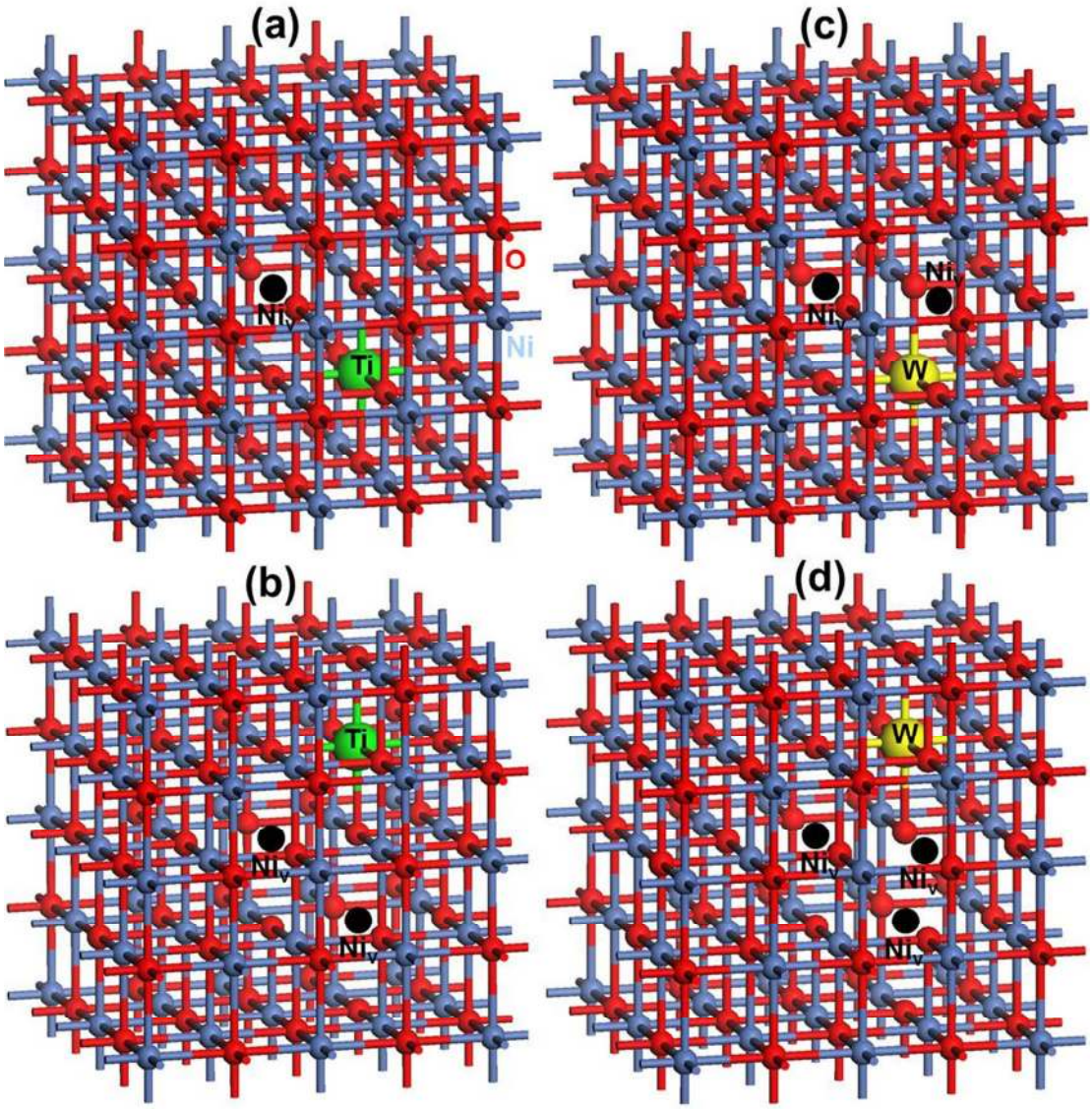

Figure 1

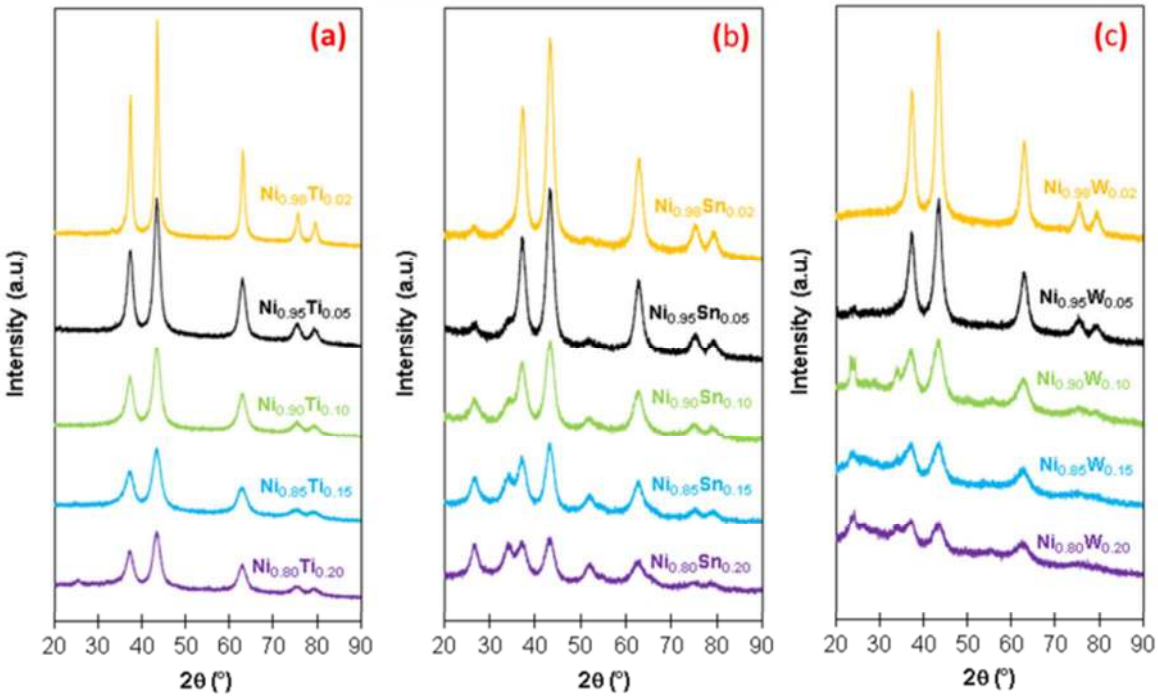
(a)
(b)
(c)
Intensity (a.u.)
2θ (°)
20 30 40 50 60 70 80 90
Ni0.98Ti0.02
Ni0.95Ti0.05
Ni0.90Ti0.10
Ni0.85Ti0.15
Ni0.80Ti0.20
Ni0.98Sn0.02
Ni0.95Sn0.05
Ni0.90Sn0.10
Ni0.85Sn0.15
Ni0.80Sn0.20
Ni0.98W0.02
Ni0.95W0.05
Ni0.90W0.10
Ni0.85W0.15
Ni0.80W0.20

Figure 2

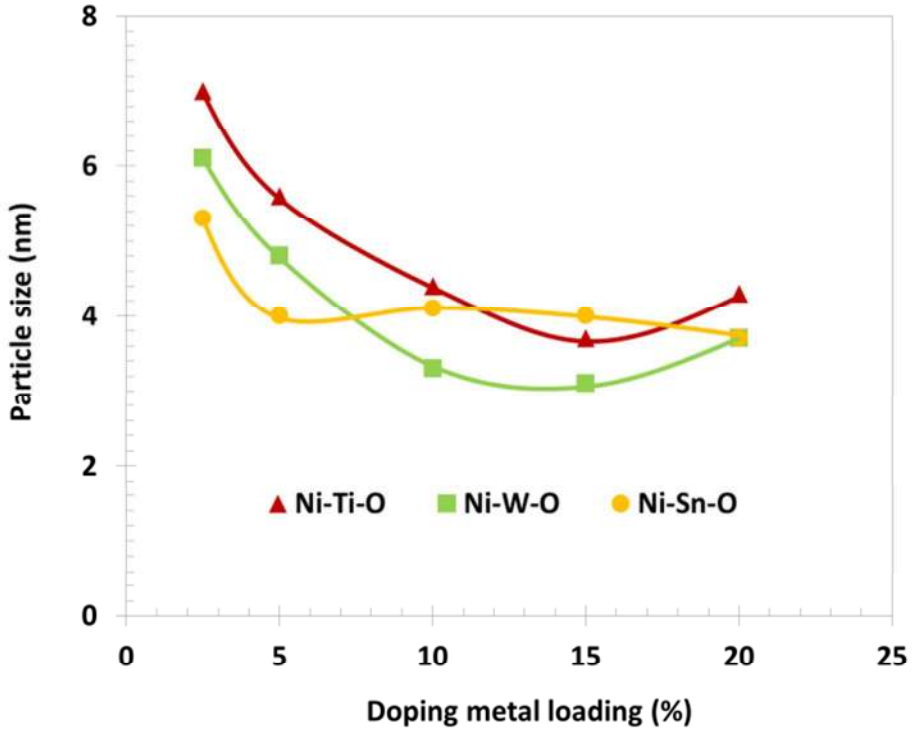
8
6
4
2
0
Particle size (nm)
0
5
10
15
20
25
Doping metal loading (%)
Ni-Ti-O
Ni-W-O
Ni-Sn-O

Figure 3

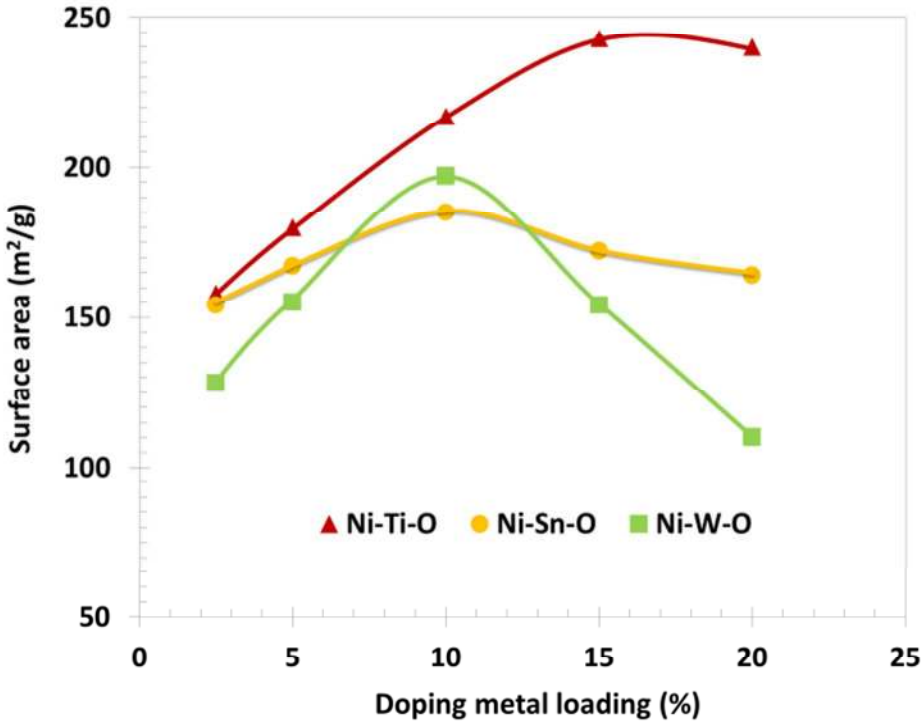
250
200
150
100
50
Surface area (m²/g)
0
5
10
15
20
25
Doping metal loading (%)
Ni-Ti-O
Ni-Sn-O
Ni-W-O

Figure 4

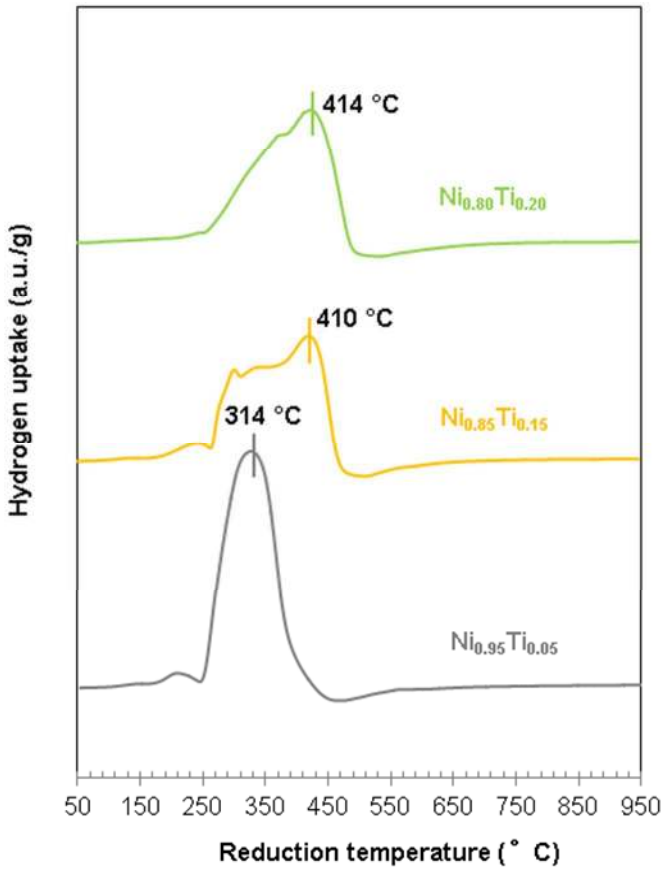
414 °C
$Ni_{0.80}Ti_{0.20}$
410 °C
314 °C
$Ni_{0.85}Ti_{0.15}$
$Ni_{0.95}Ti_{0.05}$
Hydrogen uptake (a.u./g)
50 150 250 350 450 550 650 750 850 950
Reduction temperature (° C)

Figure 5

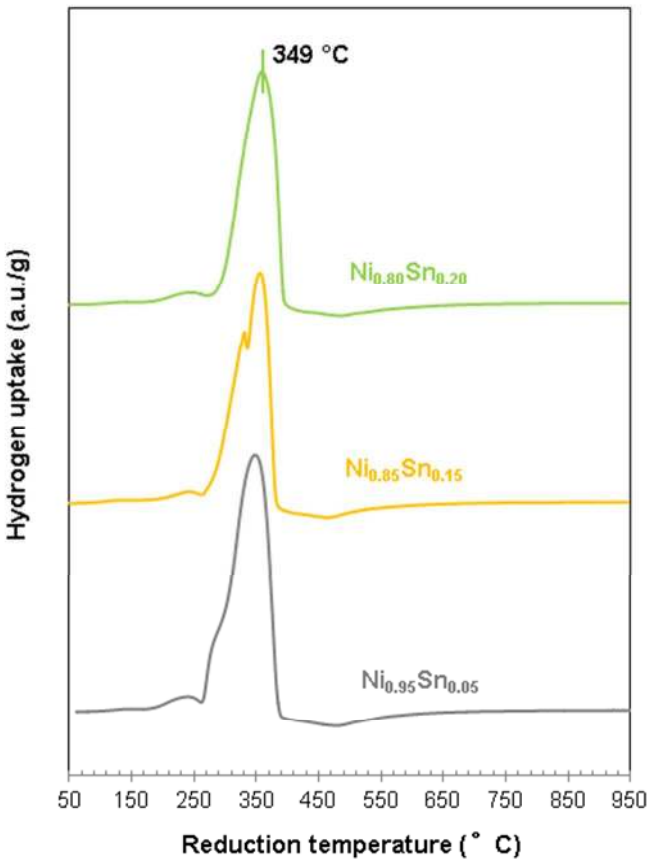
349 °C
Ni0.80Sn0.20
Ni0.85Sn0.15
Ni0.95Sn0.05
Hydrogen uptake (a.u./g)
50 150 250 350 450 550 650 750 850 950
Reduction temperature (° C)

Figure 6

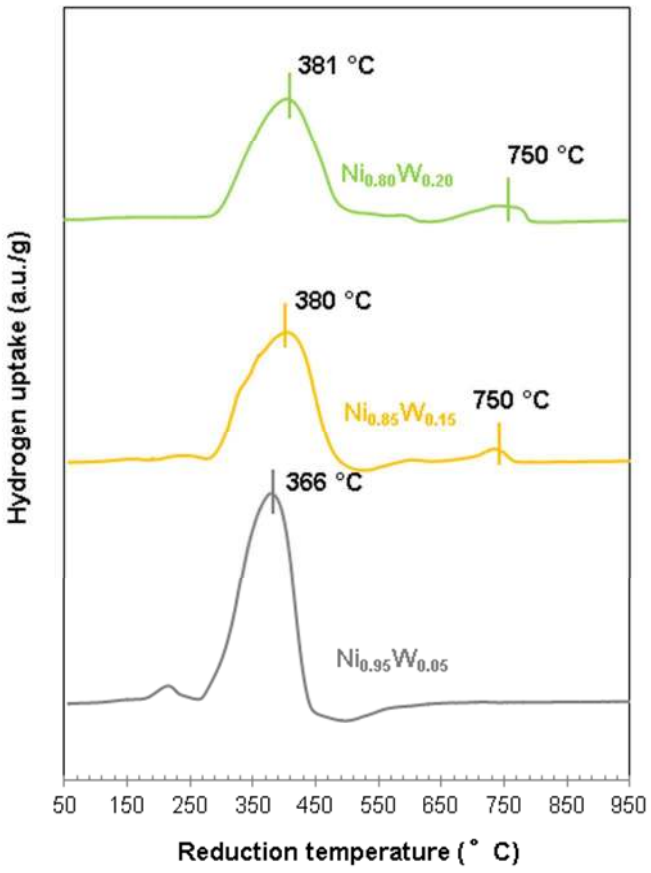
381 °C
750 °C
$Ni_{0.80}W_{0.20}$
380 °C
$Ni_{0.85}W_{0.15}$
750 °C
366 °C
$Ni_{0.95}W_{0.05}$
Hydrogen uptake (a.u./g)
50 150 250 350 450 550 650 750 850 950
Reduction temperature (° C)

Figure 7

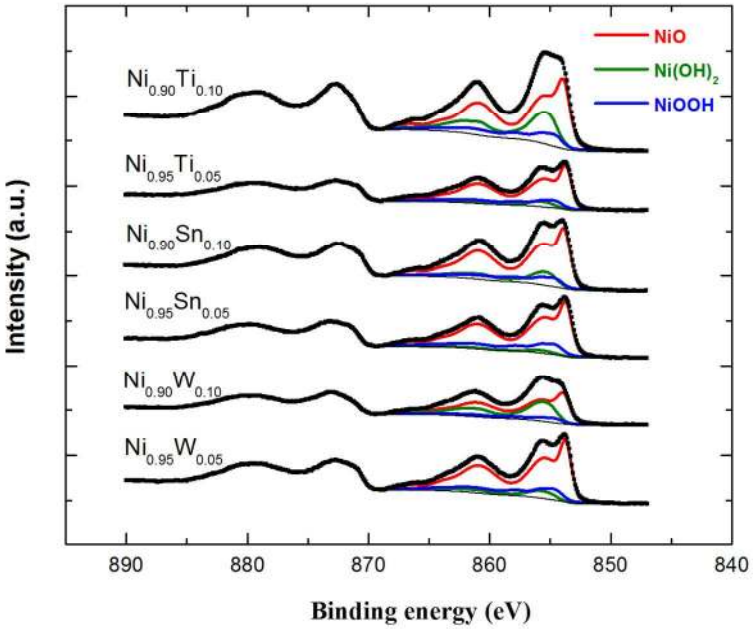
NiO
Ni(OH)2
NiOOH
Ni0.90Ti0.10
Ni0.95Ti0.05
Ni0.90Sn0.10
Ni0.95Sn0.05
Ni0.90W0.10
Ni0.95W0.05
Intensity (a.u.)
890
880
870
860
850
840
Binding energy (eV)

Figure 8

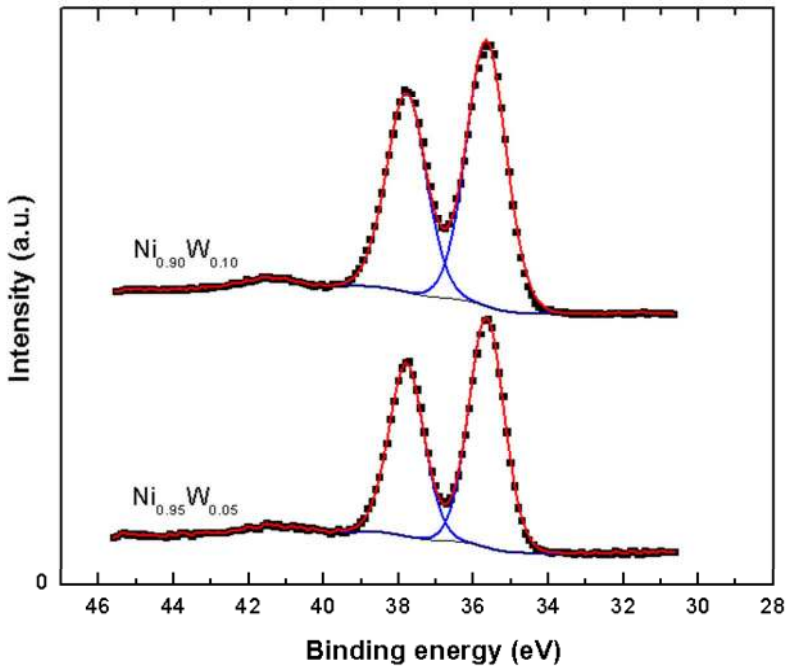
Intensity (a.u.)
Ni0.90W0.10
Ni0.95W0.05
0
46
44
42
40
38
36
34
32
30
28
Binding energy (eV)

Figure 9

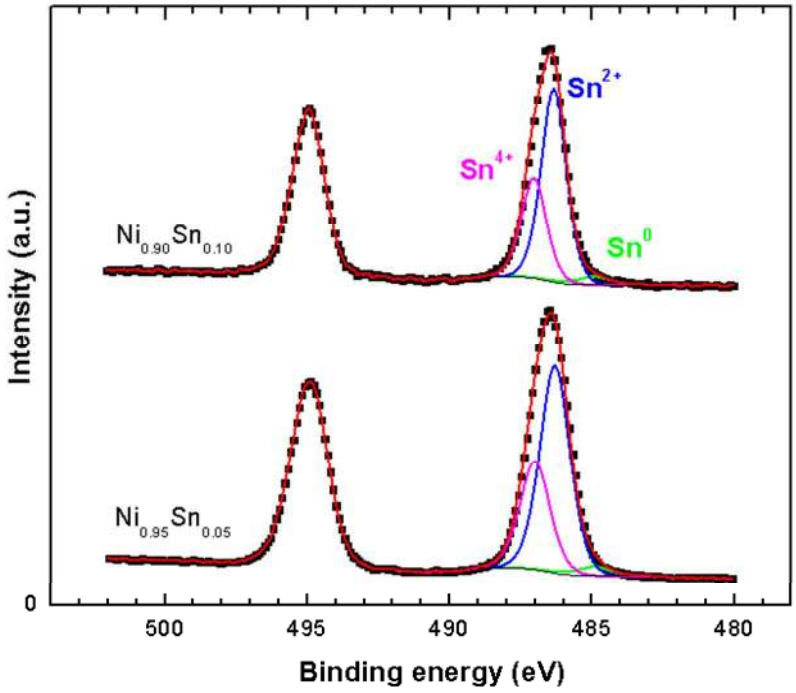
Intensity (a.u.)
Ni0.90Sn0.10
Ni0.95Sn0.05
Sn2+
Sn4+
Sn0
0
500
495
490
485
480
Binding energy (eV)

Figure 10

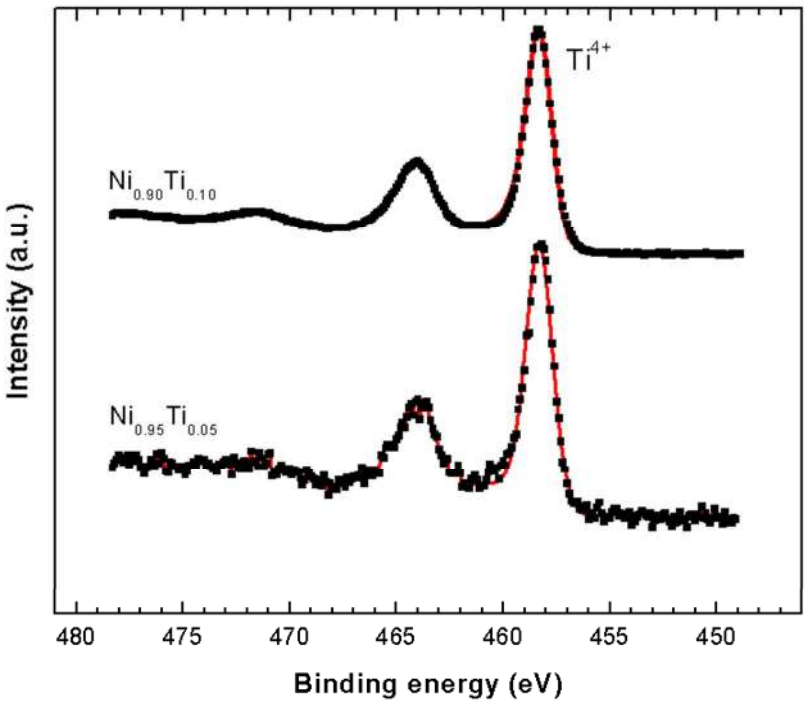
Ti4+
Ni0.90Ti0.10
Ni0.95Ti0.05
Intensity (a.u.)
480
475
470
465
460
455
450
Binding energy (eV)

Figure 11

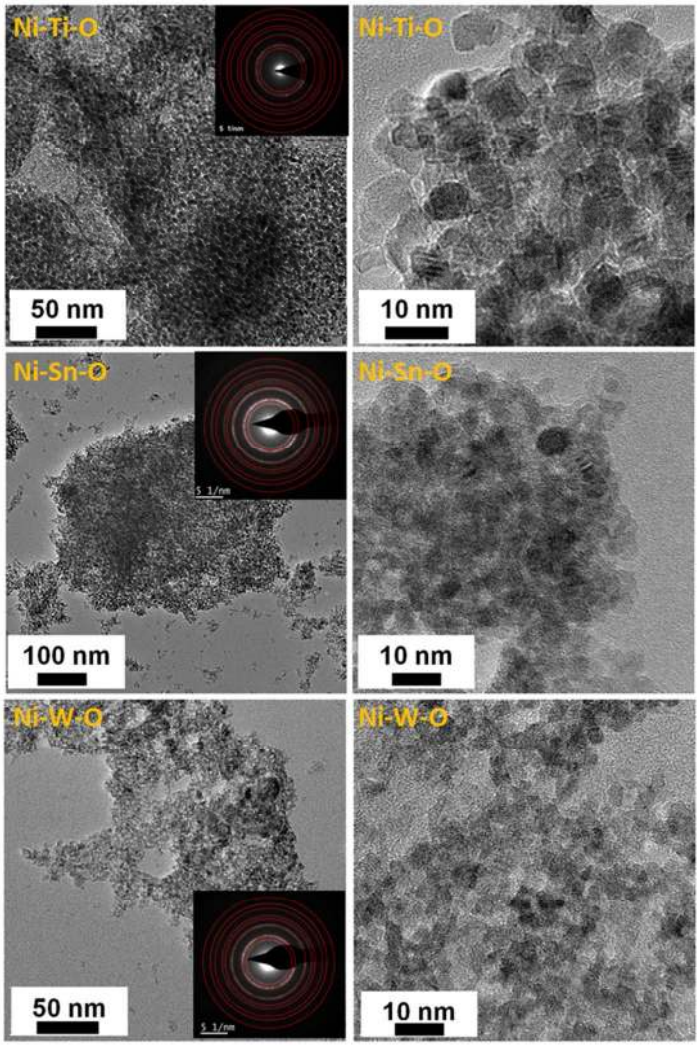
Ni-Ti-O
50 nm
Ni-Ti-O
10 nm
Ni-Sn-O
100 nm
Ni-Sn-O
10 nm
Ni-W-O
50 nm
Ni-W-O
10 nm

Figure 12

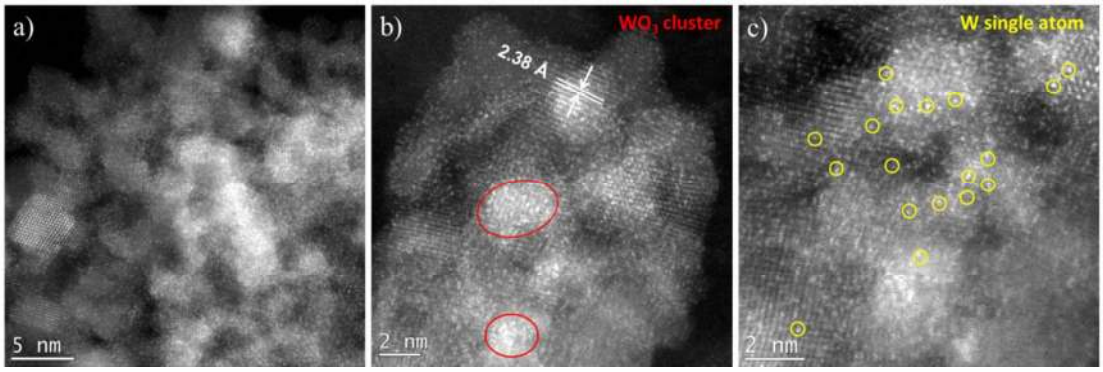

Figure 13

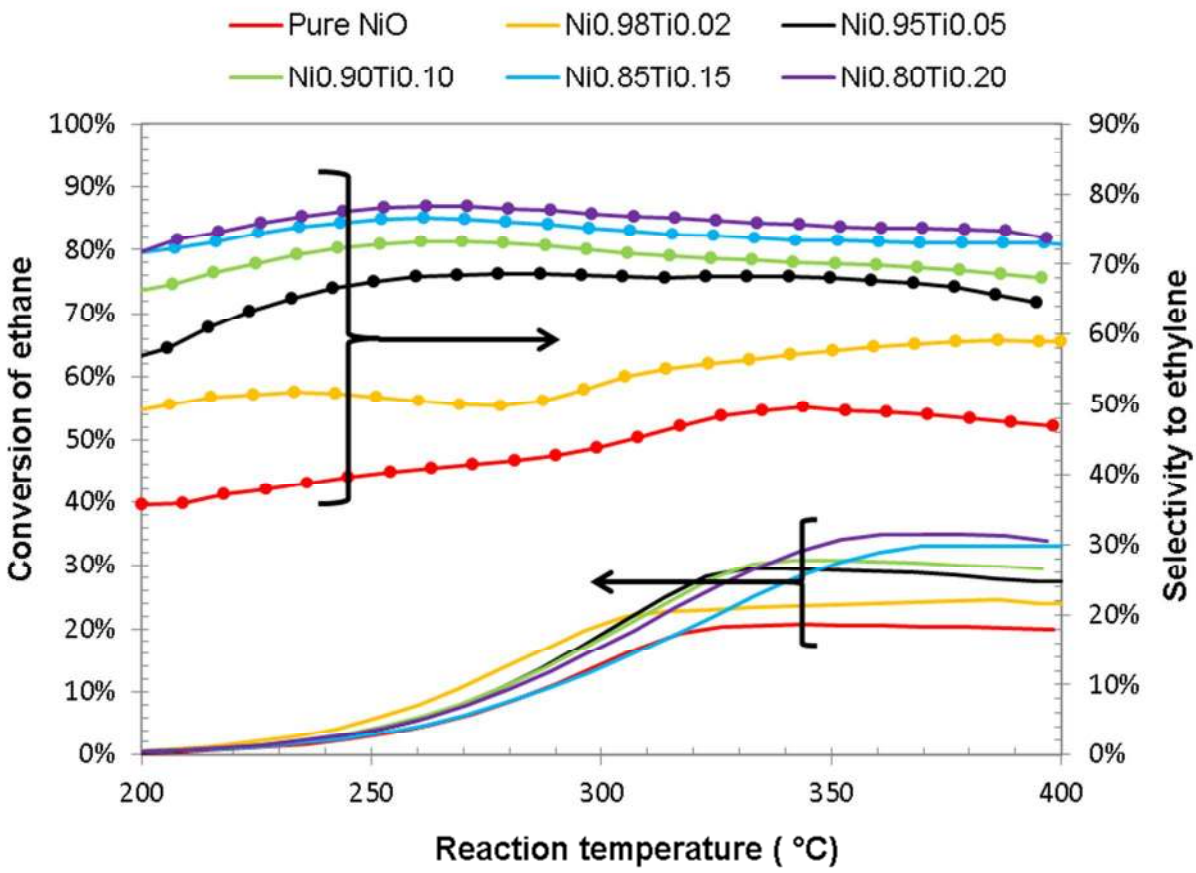
Pure NiO
Ni0.98Ti0.02
Ni0.95Ti0.05
Ni0.90Ti0.10
Ni0.85Ti0.15
Ni0.80Ti0.20
Conversion of ethane
Selectivity to ethylene
Reaction temperature (°C)
100%
90%
80%
70%
60%
50%
40%
30%
20%
10%
0%
200
250
300
350
400

Figure 14

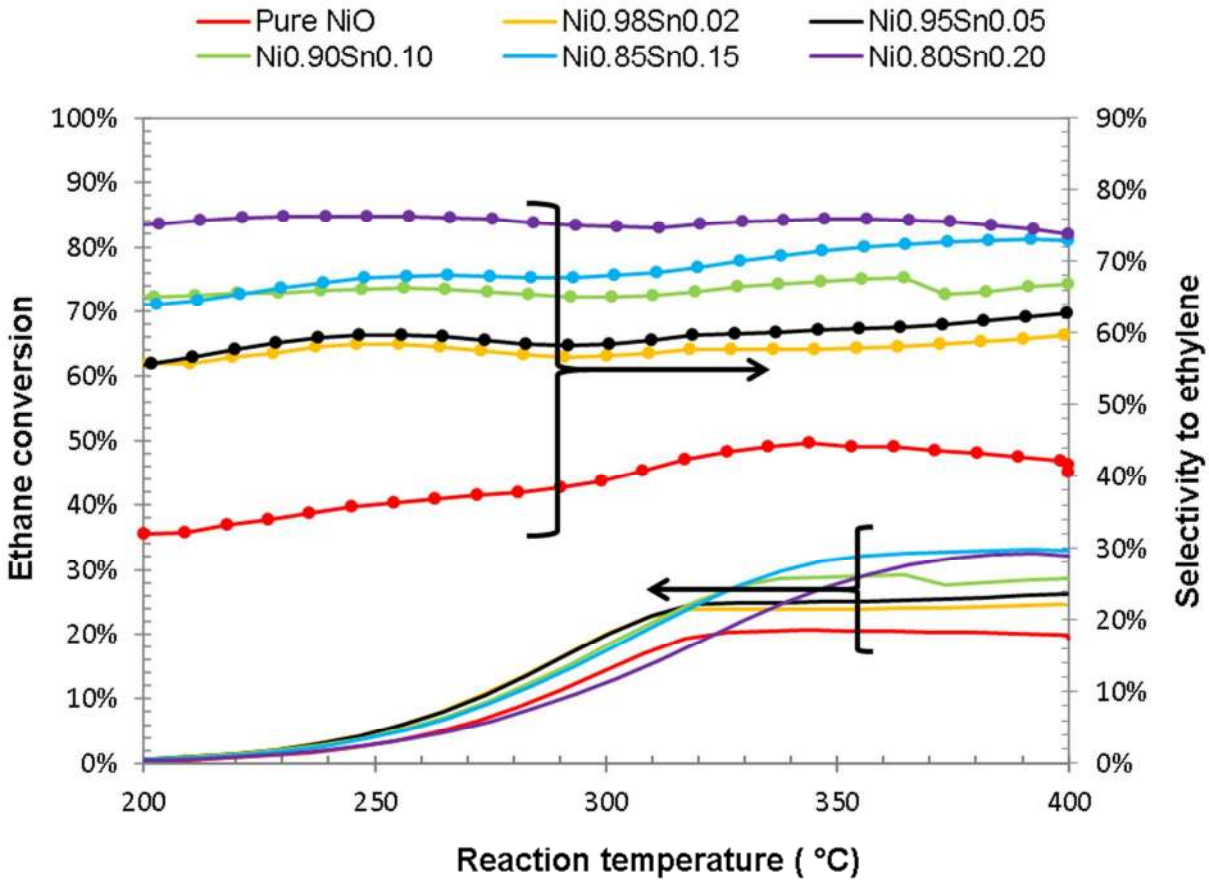
Pure NiO
Ni0.98Sn0.02
Ni0.95Sn0.05
Ni0.90Sn0.10
Ni0.85Sn0.15
Ni0.80Sn0.20
Ethane conversion
Selectivity to ethylene
Reaction temperature (°C)
100%
90%
80%
70%
60%
50%
40%
30%
20%
10%
0%
200
250
300
350
400

Figure 15

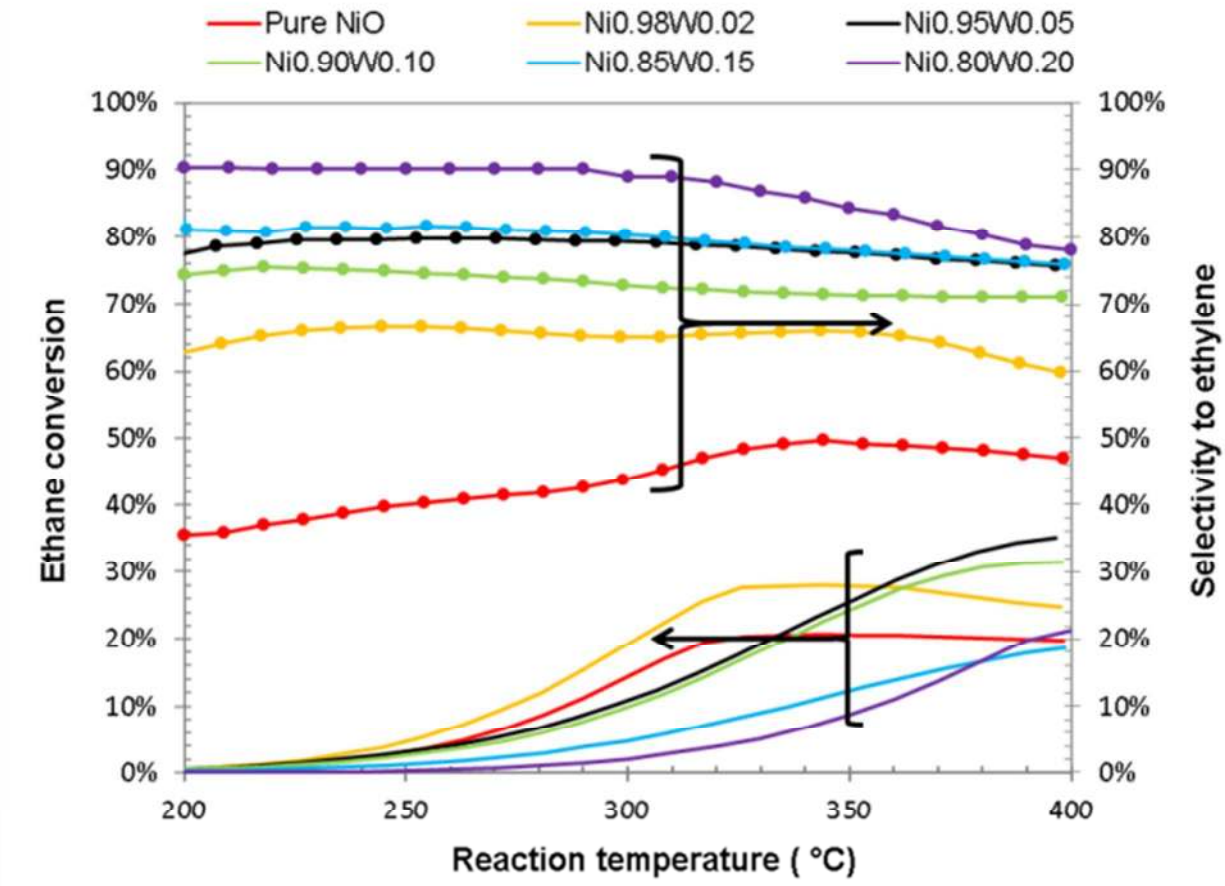
Pure NiO
Ni0.98W0.02
Ni0.95W0.05
Ni0.90W0.10
Ni0.85W0.15
Ni0.80W0.20
Ethane conversion
Selectivity to ethylene
Reaction temperature (°C)
100%
90%
80%
70%
60%
50%
40%
30%
20%
10%
0%
200
250
300
350
400

Figure 16

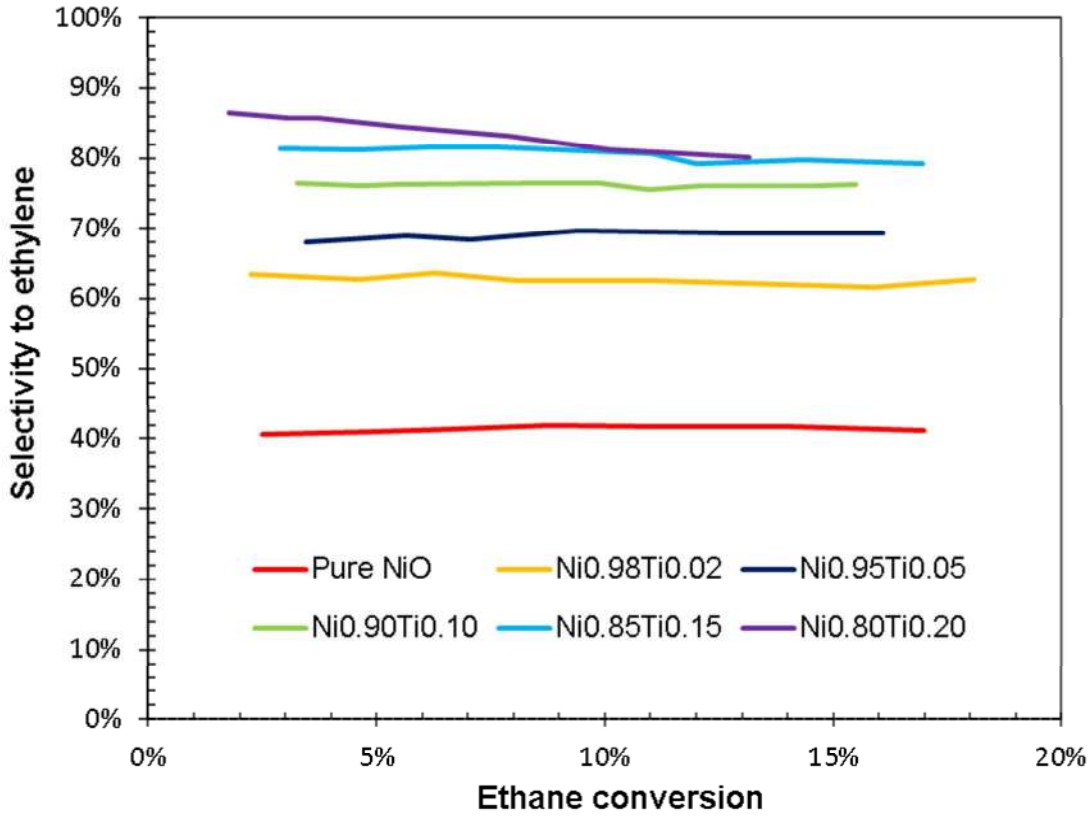
100%
90%
80%
70%
60%
50%
40%
30%
20%
10%
0%
Selectivity to ethylene
0%
5%
10%
15%
20%
Ethane conversion
Pure NiO
Ni0.98Ti0.02
Ni0.95Ti0.05
Ni0.90Ti0.10
Ni0.85Ti0.15
Ni0.80Ti0.20

Figure 17

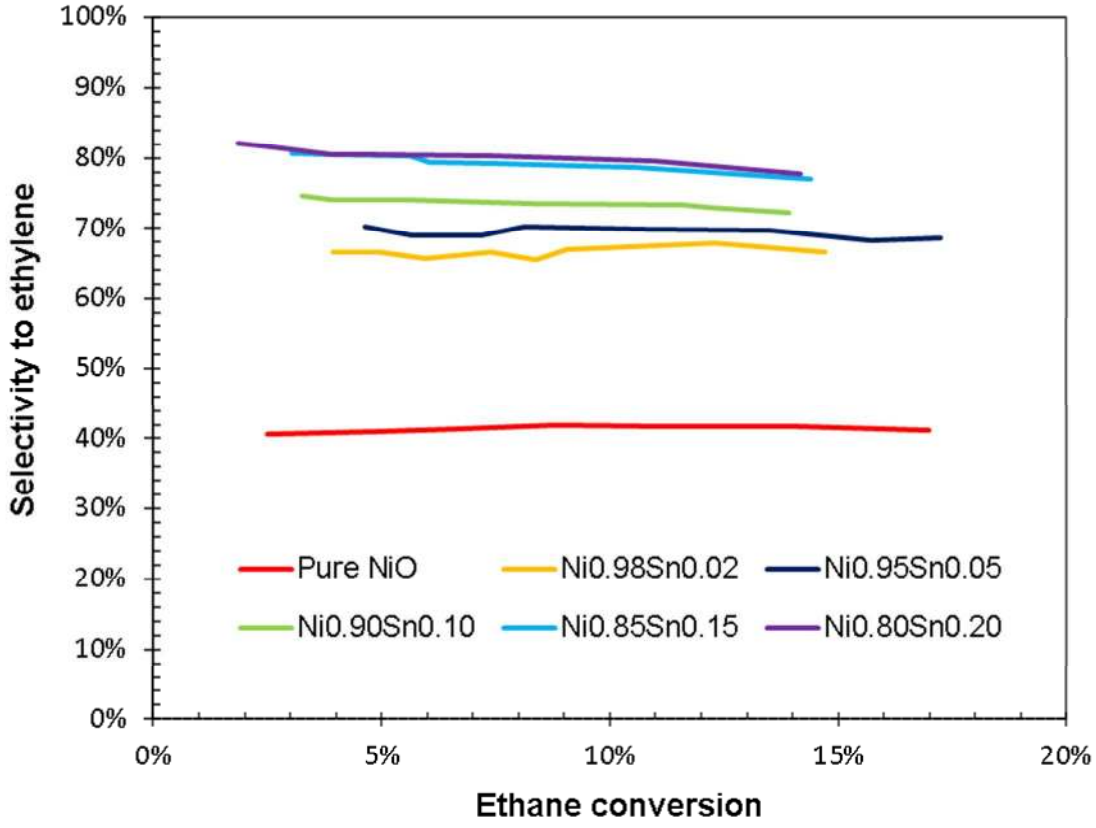
100%
90%
80%
70%
60%
50%
40%
30%
20%
10%
0%
Selectivity to ethylene
0%
5%
10%
15%
20%
Ethane conversion
Pure NiO
Ni0.98Sn0.02
Ni0.95Sn0.05
Ni0.90Sn0.10
Ni0.85Sn0.15
Ni0.80Sn0.20

Figure 18

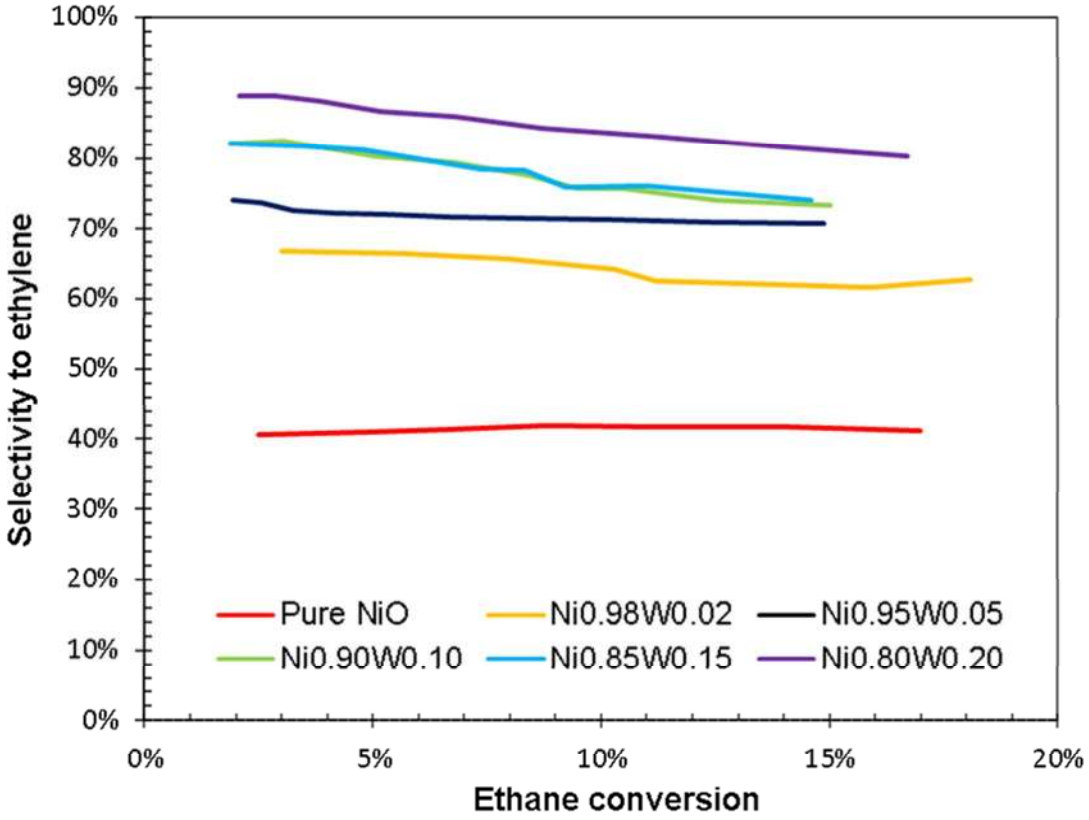
100%
90%
80%
70%
60%
50%
40%
30%
20%
10%
0%
Selectivity to ethylene
0%
5%
10%
15%
20%
Ethane conversion
Pure NiO
Ni0.98W0.02
Ni0.95W0.05
Ni0.90W0.10
Ni0.85W0.15
Ni0.80W0.20

Figure 19

Table of Contents